Pt-Anchored-Zirconium Phosphate Nanoplates as High-Durable Carbon-free Oxygen Reduction Reaction Electrocatalyst for PEM Fuel Cell Applications

Sachin Kumar,[a, b, ‡] *Athira Yoyakki,*[a, ‡] *Ajmal Pandikassala,*[a,b] *Roby Soni,*[c] *and Sreekumar Kurungout*[a,b,*]

[a] Physical and Materials Chemistry Division, CSIR-National Chemical Laboratory, Dr Homi Bhabha Road, Pune 411 008, India. E-mail: k.sreekumar@ncl.res.in

[b] Academy of Scientific and Innovative Research, Ghaziabad, 201002, India

[c] Electrochemical Innovation Laboratory, Department of Chemical Engineering, University College London, Gower Street, London, WC1E 6BT, UK

[‡] Both authors contribute equally

E-mail: k.sreekumar@ncl.res.in

Keywords: (carbon-free, fuel cell, oxygen reduction reaction, zirconium phosphate,)

Abstract: Commercially available platinum-supported carbon (Pt/C) catalysts are the most widely used oxygen reduction reaction (ORR) electrocatalysts in polymer electrolyte membrane fuel cells (PEMFCs). However, inadequate active triple-phase boundary formation and carbon oxidation in Pt/C during PEMFC operation shorten its lifetime and efficiency. In this direction, a new class of carbon-free electrocatalysts for ORR has been prepared by dispersing Pt nanoparticles on ZrP (Zirconium phosphates) nanoplates. In one case (ZrP@Pt), the Pt nanoparticles are found to be closely distributed and completely covering the ZrP nanoplates, whereas in the second case (Pt/ZrP), the Pt nanoparticles have selectively restricted dispersion along the edges of the support. ZrP as the support displays an intrinsic proton conductivity of ~ 0.5 x 10^{-4} S cm^{-1} at 70 ºC, with an activation energy (E_a) of 0.19 eV. Pt/ZrP shows better durability after 3000 start-stop cycles. The mass activity of Pt/ZrP is increased by 4.6 times compared to Pt/C, which exhibited a loss in mass activity by 1.37 times. The single-cell level validation of ZrP@Pt, Pt/ZrP and Pt/C as the electrocatalysts in PEMFC at an operating potential of 0.60 V shows the achievable current densities of 0.600, 0.890 and 0.890 A cm^{-2}.

1. **Introduction**

Among the various electrochemical energy sources, proton exchange membrane fuel cells (PEMFCs) have emerged as promising non-conventional energy devices. PEMFC is one of the potential clean energy sources that can be used for a variety of applications such as transportation, residential electricity supply, etc.[1], PEMFCs are categorized into High-Temperature Proton Exchange Membrane Fuel Cell (HT-PEMFC), operating in the temperature range of 150-180 ºC, and Low-Temperature Proton Exchange Membrane Fuel Cells (LT-PEMFCs), working in the range of 60-80 ºC.[2],[3] Both LT-PEMFC and HT-PEMFC possess significant technological challenges, mainly caused by the durability and performance characteristics of the state-of-the-art Pt-supported carbon (Pt/C) catalysts. The issue with the performance is related to the limitations in forming the active electrode-electrolyte interface ("triple-phase boundary"), whereas, the challenges related to the durability are mainly caused by the electrochemical corrosion of the carbon support of the catalysts.[4],[5] Whereas an ionomer like Nafion serves as the proton-conducting phase in the electrodes of LT-PEMFCs to create the active "triple-phase boundary", liquid phosphoric acid (H_3PO_4) immobilized in a suitable binder like polytetrafluoroethylene (PTFE) serves as the proton-conducting medium in the case of HT-PEMFCs.[6],[7] Conventionally, the electrode-electrolyte interface creation is generally accomplished through physical mixing of the catalyst and the respective ingredients as part of the electrode fabrication protocols. However, these processes cannot ensure interface formation beyond a limit, and, generally, the Pt nanoparticles deposited in the geometrically restricted areas of the carbon support such as pores and cavities will not be effectively utilized. In the case of the durability issue caused by the electrochemical carbon corrosion, mainly the operational potential, acidic pH, humid atmosphere and cell temperature are creating a fertile environments for triggering the process. [8],[9],[10] During the start-up of a fuel cell, the electrodes experience significant polarisation causing very high cathode potential up to 1.5 to 2.0 V. Further, at the anode catalytic sites, because of the fuel starvation, the requirements of necessary electrons and protons are catered by the mediation of the oxidation of the carbon.[4] In the case of HT-PEMFC, its high operating temperature, presence of liquid H_3PO_4 and steam partial pressure further accelerate the carbon corrosion process compared to LT-PEMFCs. Hence, as a direct solution to tackle the abovementioned two issues, the possibility of developing carbon-free electrocatalysts made up of suitable supports possessing intrinsic proton conductivity and strong binding affinity with Pt nanoparticles is worth exploring.

To address the aforementioned challenges, researchers have adopted different strategies based on inorganic material mediated proton conductivity enhancement of the electrolyte and the electrodes. For instance, metal oxides such as SiO_2, TiO_2, ZrO_2-TiO_2 etc. have been added to the proton conducting

membranes for improving the overall proton conductivity.[11],[12] In the case of the polybenzimidazole (PBI) membranes for HTPEMFCs, modification with metal oxides such SiO_2 resulted to a proton conductivity of 0.038 S cm^{-1} while the pristine membrane shows a proton conductivity of 0.0152 S/cm.[13] The composite membrane with 2 % TiO_2 exhibited the maximum power density of 438 mW cm^{-2} compared to the cells with the pristine membranes delivered a power density of 344 mW cm^{-2}.[14] This increase in the power density explains the capability of the TiO_2 to absorb the acid at high temperatures. Similarly, SiO_2 has been incorporated into the PBI membrane to show a similar effect as the TiO_2. The composite membrane of SiO_2 with PBI shows the power density of 0.250 mW cm^{-2} compared to the non-composite membrane exhibiting 0.185 mW cm^{-2} at 165 ºC.[13] Though metal oxides help in water and acid retention capability, they do not possess intrinsic solid-state proton conductivity such as that of zirconium phosphate.[15] Incorporation of zirconium hydrogen phosphate/zirconium phosphate (ZrP) in the Nafion® membrane exhibited ~2 times higher proton conductivity compared to the pristine Nafion® membrane.[16] ZrP also possesses desirable characteristics such as solid-state proton conductivity and high water retention capability, enabling high stability and activity in ZrP/Nafion® composite membranes for Direct Methanol Fuel Cells (DMFCs).[16] The composite membrane of Nafion® and mesoporous ZrP has been explored, which exhibits a power density of 285 mW cm^{-2} at a relative humidity of 18 % compared to the pristine Nafion membrane having a peak power density of 170 mW cm^{-2}.[17] ZrP has also been explored as the potential proton conducting material for the direct hydrocarbon polymer electrolyte fuel cells.[18] Moreover, ZrP incorporated into the catalyst layer of Pt/C in membrane-electrode-assembly (MEA) has shown much better activity and stability in HT-PEMFCs.[19] Importantly, when combined with ionic liquid, ZrP is known to enhance proton conductivity making it worth exploring for PEMFCs.[20] In addition, the phosphate group was found to strongly interact with the Pt, thereby enhancing the stability of the dispersed state of Pt.[21]

Considering the important functional attributes of ZrP due to its solid-state proton conductivity, in this work, we tried to explore the possibility of utilizing ZrP in the form of nanoplates as a non-carbonaceous support for dispersing Pt nanoparticles and evaluate the performance towards oxygen reduction reaction (ORR). Since the phosphate groups in ZrP possess acidic functionality, the intimate contact between the Pt nanoparticles and phosphate group of the ZrP is expected to benefit the active interface. In addition, the surface phosphate functionality has the ability to modulate the activity and the stability of the Pt nanoparticles for the oxygen reduction reaction (ORR). The results discussed in the manuscript, including the single-cell demonstrations of the PEMFCs derived from the ZrP-based electrodes, point towards the interesting ORR performance of the ZrP derived non-carbonaceous electrocatalysts for PEMFC applications with ability to alleviate the issues associated with the carbon corrosion.

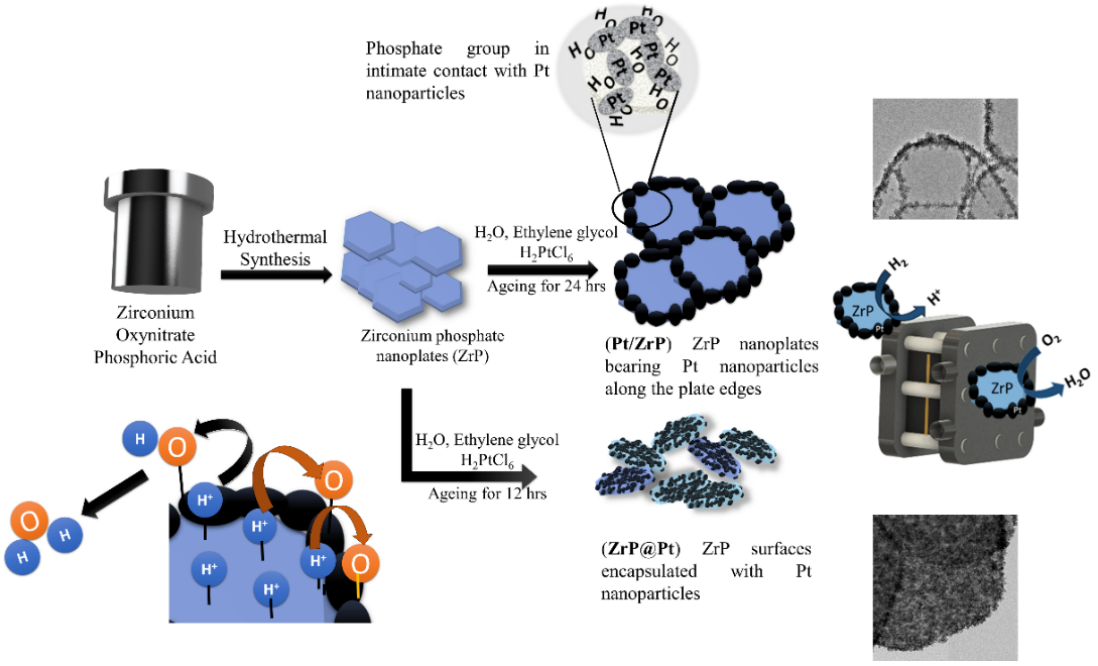

Scheme 1. Schematic representation of the steps Involved in the synthesis of the Pt supported ZrP nanoplates. Two types of Pt dispersed catalysts are derived, where, in one case, the Pt nanoparticles are dispersed only along the outer edges of the ZrP nanoplates (Pt/ZrP) and, in the other case, the ZrP nanoplates are completely encapsulated by a coverage of closely dispersed Pt nanoparticles throughout their surface (ZrP@Pt).

2. Results and Discussion

Scheme 1 illustrates the procedures followed for the synthesis of ZrP and its decoration by Pt on the surface (ZrP@Pt) as well as on the edge sites of ZrP (Pt/ZrP). The comparative XRD profiles recorded for ZrP, ZrP@Pt, and Pt/ZrP are shown in **Figure 1**. The peaks appeared in the case of ZrP at the 2Θ values of 11.27°, 19.48°, 24.61°, and 33.50° are ascribed to the (002), (110), (112) and (020) planes of ZrP and thus confirms its alpha-phase.[22] In the case of ZrP@Pt, the diffraction peaks at 11.27°, 19.52°, 24.69°, and 33.61° correspond to the (002), (110), (112) and (020) planes of ZrP, whereas, the peaks at 39.40° and 46.6° represent the (111) and (200) planes of Pt. [23] Further, a decrease in the peak intensities corresponding to the ZrP phase has been observed in the case of ZrP@Pt, and this can be attributed to the surface coverage of the substrate by the Pt nanoparticles. Compared to the pristine ZrP and ZrP@Pt, the peaks corresponding to the planes of ZrP are found to be broad in the case of Pt/ZrP. This points towards the amorphization of ZrP, possibly caused by the extended aging duration of 24 h involved during the catalyst synthesis. Further, the appearance

of the diffraction peaks at the 2Θ values of 39.8°, and 46.94° represents the presence of the Pt (111) and Pt (200) planes.[23]

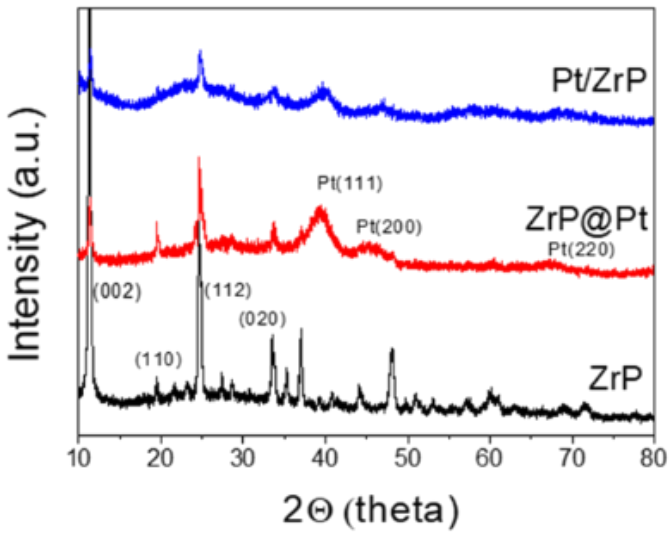

Figure 1. The comparative XRD profiles recorded for ZrP, ZrP@Pt and Pt/ZrP.

The morphological characteristics of the as-synthesized ZrP, ZrP@Pt, and Pt/ZrP are initially investigated with the help of FE-SEM analysis (**Figure 2a-c)**. The FE-SEM image of ZrP, as depicted in **Figure 2a**, displays the formation of well-separated nanoplates of the substrate with hexagonal morphology. The average diameter of the ZrP nanoplates is estimated to be around 400 nm, with the edge length varying from 35 to 50 nm (inset, **Figure 2a**). **Figure 2b** shows the image of ZrP@Pt, where, the Pt nanoparticles are decorated over the entire surface of the ZrP nanoplates. It is clear from the rough patches and dotted pattern that the Pt nanoparticles are uniformly distributed over the surface of ZrP in ZrP@Pt. Similarly, the FE-SEM analysis shows a peculiar type of dispersion characteristics of Pt in Pt/ZrP, wherein the Pt particles are appeared to be selectively located at the edges of the nanoplates of ZrP (**Figure 2c**).

We hypothesize that the difference in the nature of the Pt decoration, of one involving along the entire surface of ZrP (ZrP@Pt) and the second case of dispersion selectively along the edges of the substrate (Pt/ZrP), is possibly caused by the surface modification of the ZrP due to difference in the aging time. In the case of ZrP@Pt, where the Pt nanoparticles are decorated over the surface of the ZrP, the hydroxyl groups are well oriented along the zirconium phosphate (ZrP) surface. Hence, the nucleation takes place over the surface as shown in **Figure S1** by the intervention of the hydroxyl groups and the Pt ions. On the other hand, in the case of Pt/ZrP, due to the semi-crystalline or amorphous nature of ZrP which occurs due to the dissolution of ZrP surface, the nucleation takes place along the edges of ZrP. This is further confirmed with the help of the TEM and HR-TEM analyses of ZrP without aging (0 h) and aged for 12 and 24 h. The surface modification of ZrP aged for 24 h shows more prominent circular patches than the ZrP without

aging and that aged for 12 h **(Figure S2)**. Hence, the Pt decoration is restricted mainly to the edges of ZrP (**Figure S1**). The phosphate group on the edges is more reactive than the inner region because of the "dangling" P-O or P-OH group[24] and in the case of the aged solution, the hydroxyl group cannot coordinate with the chloroplatinic acid. Hence, after 24 h of the aging process, the Pt species coordinate with the edges, and nucleation only takes place along the edges. The mechanism for the Pt nanoparticle coordination along the edges and over the surface of the ZrP is further given in Figure S1.

TEM analysis of the ZrP nanoplates shown in **Figure S2a-d** reveals the smooth surface finish and hexagonal morphology of the plates. More insightful information on the nature of the decoration of the Pt nanoparticles on the surface of the ZrP in the case of ZrP@Pt and Pt/ZrP could be gained by the TEM analysis and the corresponding data are presented in **Figure 3a-f. Figure 3a-c** clearly show that uniformly sized Pt nanoparticles are exclusively located at the edges of the ZrP nanoplates (Pt/ZrP). Also, a close look at the distribution pattern reveals that the Pt nanoparticles are interconnected in nature even though the spherical shapes of the individual particles are retained without any indication of agglomeration or merging of the boundaries. In contrast, the Pt nanoparticles in ZrP@Pt cover the entire surface of the nanoplates of ZrP with a layer of more closely distributed particles (**Figure 3d-f**). This close distribution of the Pt nanoparticles on the entire surface of ZrP essentially covers the substrate and acquires a core-shell type distribution profile in the case of ZrP@Pt. The relatively high intensity of the Pt peaks in the XRD profile in **Figure 1** with a concomitant reduction in the intensity of the peaks corresponding to ZrP is in agreement with the morphological feature revealed through the TEM analysis. The Pt nanoparticles decorated either at the edges (Pt/ZrP) or over the surface (ZrP@Pt) of the ZrP exhibit interconnectivity with inter-grain boundaries that enhance the conductivity and charge transfer, thereby modulating the electrocatalytic activity of the Pt nanoparticles.[30] The average size of the Pt nanoparticles in both the systems is estimated to be around 2.0-2.5 nm, with a d-spacing value of around 0.216 nm (**Figure S3**).This corresponds to the Pt(111) plane, further confirming the metallic nature of the Pt nanoparticles.[25]The distribution of the elements in Pt/ZrP and ZrP@Pt was further characterized by energy-dispersive X-ray spectroscopy (EDX). The EDX mapping (**Figure S4 a-h**) clearly reveals the presence of the Zr, O, P and Pt, further supporting the distinct nature of the distribution profiles of Pt in Pt/ZrP and ZrP@Pt.

It is evident from the TEM data that the Pt nanoparticles are formed in an interconnected manner, which might be responsible for achieving the electron conduction even though the the support is not electrically conductive.[26] To further confirm the nature of the electronic conductivity of ZrP and the Pt-decorated ZrP, the I-V polarisation plots were recorded, and the corresponding data are presented in **Figure S5**. The measurement validates that the formation of the interconnected network of the Pt nanoparticles on the substrate is aiding electronic conductivity and resulted into a value of 8.5 S cm^{-1}. The obtained value

conforms with the electrical conductivity values reported on some Pt-deposited metal oxides.[27] This strategy of overcoming the conductivity related drawbacks of the metal oxide type substrates with the help of forming a surface layer of a conductive species has already been practiced in electrochemical systems, including PEMFCs.[28] We have compared the electronic conductivity of the materials as given in **Table S1**. It can be seen that the ZrP, which is not electronic conductive as such, is becoming conductive subsequent to the Pt decoration along the edges or over the surface.

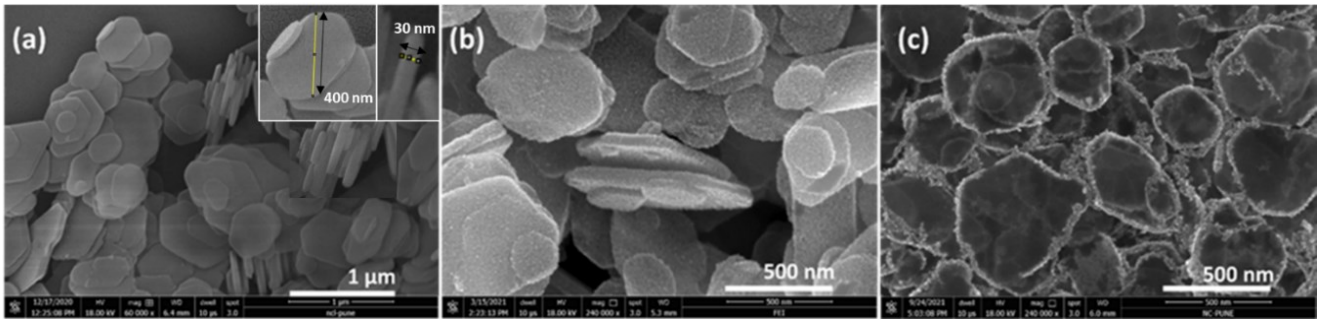

Figure 2. The FE-SEM images of (a) ZrP nanoplates, (b) ZrP@Pt, and (c) Pt/ZrP. In the case of ZrP@Pt, the Pt nanoparticles are found to be closely distributed and completely covering the ZrP nanoplates, whereas in Pt/ZrP, the Pt nanoparticles have selectively restricted dispersion along the edges of the support.

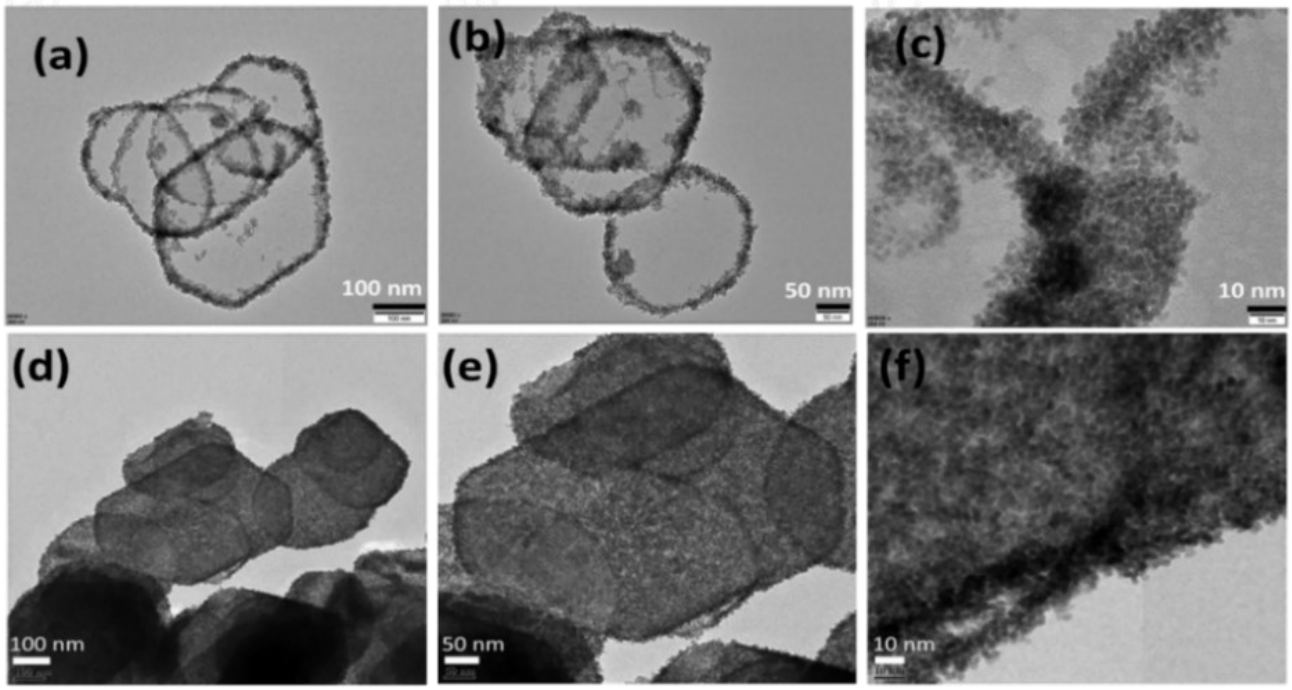

Figure 3. The TEM images recorded at different magnifications of (a-c) Pt/ZrP displaying the Pt decoration selectively along the edges of the ZrP nanoplates, and (d-f) ZrP@Pt having the Pt nanoparticles decorated over the entire surface of the nanoplates of ZrP.

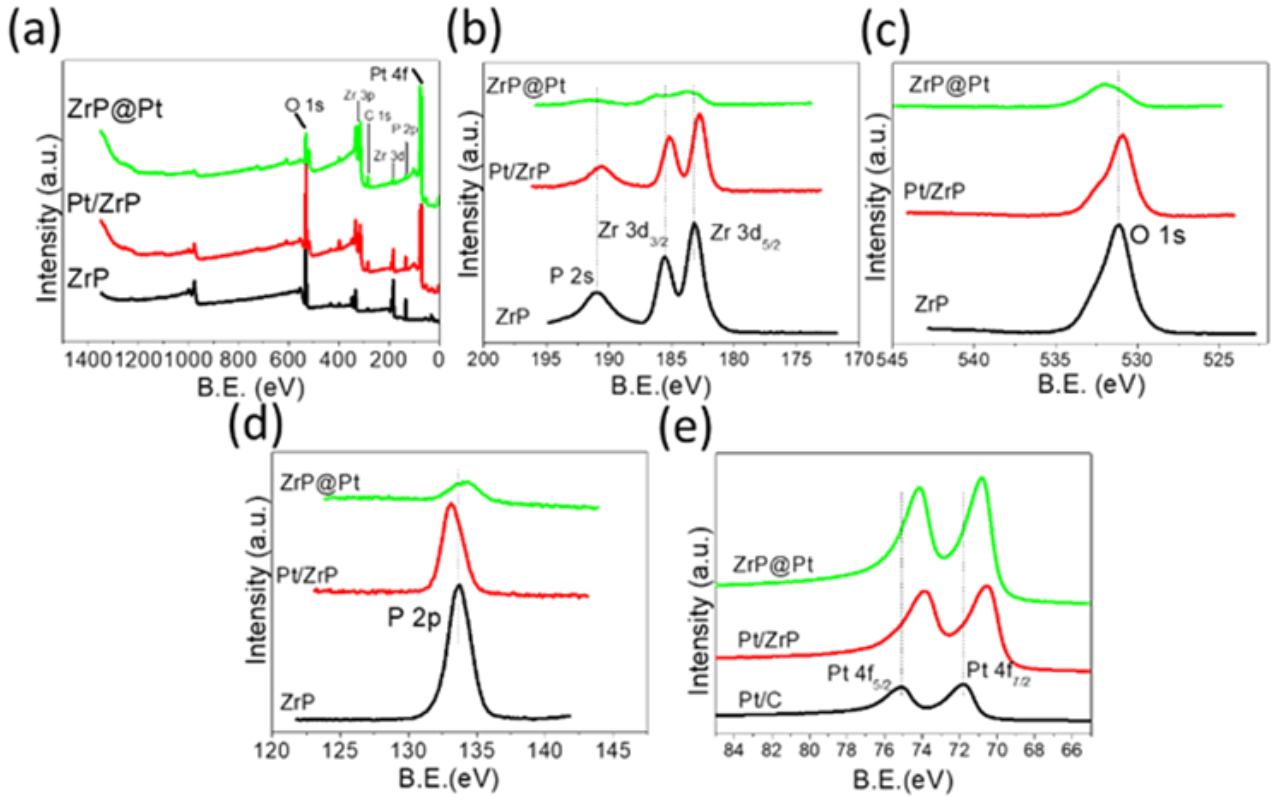

Figure 4. The XPS profiles of ZrP, Pt/ZrP and ZrP@Pt: (a) the comparative survey spectra of the samples; (b-e) the XPS core spectra of Zr 3d (b), O 1s (c), P 2p (d), and Pt 4f (e).

To further look into the oxidation states of the different involved species in the catalyst systems and the possible electronic modifications due to their coexistence, X-ray Photon Spectroscopy (XPS) was performed. XPS survey spectra of ZrP, ZrP@Pt, and Pt/ZrP given in **Figure 4a** confirm the presence of Zr, P, O, and Pt in the respective systems. The core level XPS spectra of the Zr 3d show the two separate regions *viz*, Zr $3d_{3/2}$ and Zr $3d_{5/2}$ due to spin-orbital coupling. The binding energy values of Zr $3d_{3/2}$ and Zr $3d_{5/2}$ in the pristine ZrP are 185.5 and 183.2 eV, respectively.[29] The BEs for Zr $3d_{3/2}$ are 186.15 and 185.19 eV, respectively, for ZrP@Pt and Pt/ZrP, whereas, the peaks corresponding to $Zr3d_{5/2}$ are appeared at 183.85 and 182.79 eV, respectively for both the samples. **Figure 4c** represents the BE plots corresponding to the O 1s state in ZrP, ZrP@Pt and Pt/ZrP, where the peaks appear at 531.1, 532.05 and 530.89 eV, respectively.[30]The observed positive shift in the BE for O 1s in ZrP@Pt further validates the strong Pt-O interaction operating in the system. Further, the P 2p core spectra as presented in **Figure 4d** show the peaks at 133.7 and 133.95 eV for ZrP and ZrP@Pt, respectively.[22]The higher BE value recorded for ZrP@Pt clearly points towards the existence of the strong Pt-P interaction in the system. In contrast, the observed BE corresponding to the P 2p state for Pt/ZrP is only 133.09 eV. Thus, the distinct differences observed in

the binding energy values corresponding to the Zr 4f, O 1s, and P 2p states in the case of ZrP@Pt and Pt/ZrP can be taken as a proof for the differences existing in these two systems in terms of the interaction of the

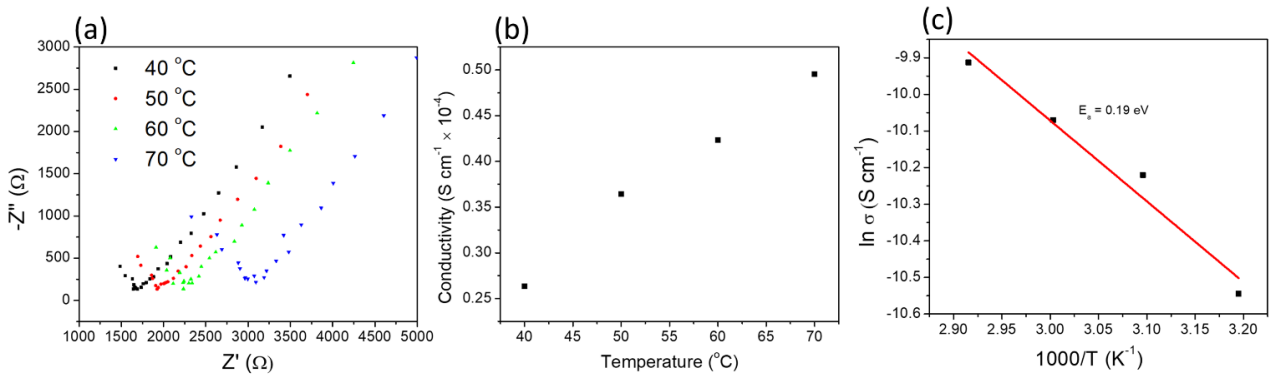

Figure 5. (a) The Nyquist plots recorded for ZrP as a function of temperature and 95 % relative humidity, (b) the plot indicating the proton conductivity as a function of temperature of the ZrP nanoplates recorded at 95 % humidity, and (c) the Arrhenius plot constructed for calculating the activation energy (E_a) for proton conduction of the ZrP nanoplates.

Pt nanoparticles with the ZrP surface. This difference between the two systems plays as a critical deciding factor in achieving two significantly different types of the dispersion characteristics of the Pt nanoparticles on the substrate.

Similar to the Zr 3d, the Pt 4f core spectra exhibit two distinct peaks, *viz*. Pt $4f_{5/2}$ and Pt $4f_{7/2}$ due to the spin-orbital coupling. Note that, the Pt 4f peaks in the case of ZrP@Pt have been shifted to low binding energies ($4f_{5/2}$ at 74.15 eV and $4f_{7/2}$ at 70.85 eV), compared to the Pt peaks in Pt/C ($4f_{5/2}$ at 75.09 eV and $4f_{7/2}$ at 71.79 eV).[31] Similarly, in the case of Pt/ZrP, the BEs for Pt $4f_{5/2}$ and Pt $4f_{7/2}$ appear at 73.89 and 70.49 eV, respectively (**Figure 4e**). Lowering of the BEs of Pt in the case of ZrP@Pt and Pt/ZrP compared to the Pt/C further confirms the existence of the strong metal-support interactions (SMSI).[32],[33]It is evident from the Pt 4f BE values that the interaction of Pt with ZrP in Pt/ZrP is much stronger than that in ZrP@Pt. The change in the BE values of Pt 4f in the ZrP systems might be due to the different coordinating environments of the Pt nanoparticles. The charge transfer between ZrP and Pt shifts the d-band centre of Pt 4f to the lower energy. [30] This leads to the variation in the adsorption strength of the oxygen/oxygen intermediates and can lead to the improved catalytic activity for ORR. [34]

As mentioned previously, one important functional attribute of ZrP is the solid-state proton conductivity of the material. This feature of ZrP has an added advantage while employing the ZrP-based catalysts for PEMFC applications for aiding proton transport during the electrode processes. Using electrochemical impedance spectroscopy (EIS), the proton conductivity of ZrP has been measured as a function of

humidification and temperature. The typical Nyquist plots recorded at different temperatures under 95 % relative humidity (RH) are presented in **Figure 5a.** The Nyquist plots clearly display a trend showing the temperature-assisted conductivity enhancement at fixed humidity conditions.

The conductivity values vary from 0.26 x 10^{-4} S cm^{-1} to 0.50 x 10^{-4} S cm^{-1} within the temperature range from 40 to 70 ºC at 95 % humidity (Figure 5.b) (see Supporting Information for the calculations).[20] At higher temperatures, the water molecules become more mobile, thereby improving the proton conductivity of the system dramatically. Based on the temperature-dependent conductivity profiles of ZrP as presented in Figure 5c, the activation energy (E_a) for proton conductivity in ZrP has been estimated to be 0.19 eV, implying to the Grothuss mechanism.[35] The measured E_a value of ZrP is found to be similar to that of Nafion (E_a= 0.16 ± 0.02 eV).[36] The dispersion of Pt nanoparticle on the substrate possessing intrinsic proton conductivity can help in favouring the kinetics of the electrode reactions due to the direct involvement of protons in the anode as well as the cathode of PEMFCs.

The prepared catalysts were further evaluated for understanding their intrinsic activity towards electrochemical oxygen reduction reaction (ORR). A set of experimental tools including cyclic voltammetry (CV), rotating disk electrode (RDE), and rotating ring disk electrode (RRDE) were used for screening the catalysts for ORR and the studies were performed in 0.1 M $HClO_4$ as the electrolyte. The CV profiles of ZrP@Pt and Pt/ZrP recorded in nitrogen saturated electrolyte in comparison to the corresponding plot generated in the case of the state-of-the-art 40 wt.% Pt/C are presented in Figure 6a. The typical characteristics of the Pt under the acidic pH conditions with the well-defined redox peaks corresponding to the under-potential H-adsorption and desorption in the potential region of 0 to 0.30 V *vs* RHE is evident in the CV profiles of ZrP@Pt and Pt/ZrP. The peaks that appeared in the potentials of 0.13 and 0.22 V can be attributed to the hydrogen desorption from the (110) and (100) step sites of the Pt, respectively.[28] The EDAX analysis indicates a Pt loading of ~ 32 and 35 wt. %, respectively, in the case of Pt/ZrP and ZrP@Pt (**Figures S6 and S7**). During the synthesis of the Pt/ZrP, the surface layer of the Pt/ZrP, ZrP gets dissolved and semi-crystallinity appears during the aging process. This can be seen clearly in the TEM and HR-TEM images of the ZrP aged at different times, where small patches can be seen at 24 h; also, the thickness of ZrP nanoplates is noticed to be becoming reduced, as seen clearly from the FE-SEM images. While in the case of ZrP@Pt, there is no dissolution of ZrP and the surface remains as such. We hypothesize that during the synthetic process, the ZrP surface gets modified and leads to Pt decoration along the edges of ZrP. The phosphate group on the edges is more reactive than the inner region because of the "dangling" P-O or P-OH group. We performed the XRD analysis by aging the samples at 12, 16, 20, and 24 h (**Figure S8**). The hydrogen desorption region in the CV was used for calculating the electrochemical surface area (ECSA) of

the catalysts; the measured ECSA values are 33 m^2gPt^{-1} for ZrP@Pt, 32 m^2gPt^{-1} for Pt/ZrP, and 50 m^2gPt^{-1} for Pt/C. The extended interconnectivity of the Pt nanoparticles along the edges of ZrP in the case of Pt/ZrP and over the entire surface of the substrate in the case of ZrP@Pt is possibly the reason for the relatively low ECSA recorded on these systems compared to Pt/C, where the Pt nanoparticles normally do not show the interconnected nature of the dispersion characteristics.

Even with the reduced ECSA, the homemade catalysts display some interesting trends towards the ORR performance and electrochemical durability. In the case of the carbon-based catalysts, the electrochemical corrosion of the carbon substrate under the operating conditions of the cells causes progressive loss in the ECSA with a concomitant reduction in the ORR performance. This has been cited as one of the major limitations of the existing PEMFC catalysts. Since both Pt/ZrP and ZrP@Pt are based on the carbon-free substrates, these systems are found to be better surviving under the corrosive environments and thus display the prospects for performance dividends on long run compared to their carbon-based counterparts. To effectively unravel few such meritorious aspects of the homemade catalysts, an assessment on the intrinsic ORR performance characteristics has been done by recording linear sweep voltammograms (LSVs) under oxygen-enriched conditions; the corresponding LSV profiles are presented in Figure 6b. The onset and half-wave ($E_{1/2}$) potentials are the two important performance indicators pointing towards the intrinsic ORR characteristics of the electrocatalysts. The measured onset potential and $E_{1/2}$ values are respectively 0.97 and 0.81 V for Pt/C, 0.96 and 0.77 V for ZrP@Pt, and 0.97 and 0.80 V for Pt/ZrP, where the Pt loading in all the catalysts is approximately 40 wt.%. More positive onset potential and $E_{1/2}$ values of Pt/ZrP compared to ZrP@Pt can be attributed to strong electronic interaction between ZrP and Pt as evidenced from the XPS data, which results in favorable activity modulations with respect to the ORR performance. We have already seen from Figure 4e that the significant lowering of the Pt 4f BE values in the case of Pt/ZrP is caused by the charge transfer from ZrP to Pt. This can directly affect the strength of adsorption of the oxygen and oxygen intermediates, which is found to be working in favour of Pt/ZrP as reflected from the more positive shifts of the onset potential and $E_{1/2}$ values. However, compared to Pt/ZrP, the counterpart ZrP@Pt possesses better active site density per unit area due to the coverage of Pt throughout the surface of ZrP compared to Pt/ZrP, where the Pt distribution is restricted only along the edges of the substrate. This

difference is reflected in terms of the better limiting current density obtained for ZrP@Pt, which is found to be reaching gradually to the value recorded on Pt/C (5.5 mA cm^{-2}).

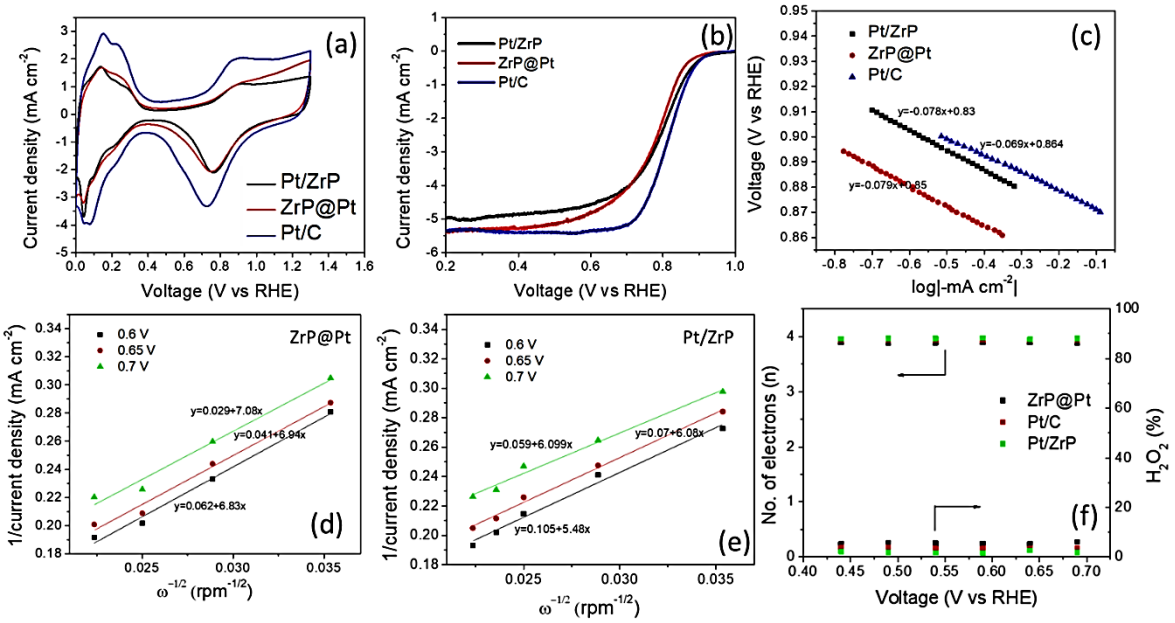

Figure 6. (a) The cyclic voltammograms (CVs) recorded for Pt/ZrP, ZrP@Pt, and Pt/C at a scan rate of 50 mV s^{-1} in N_2 and O_2 saturated environments in 0.1 M $HClO_4$ electrolyte; (b) a comparison of the LSV profiles for the samples recorded with a scanning rate of 10 mV s^{-1} and the working electrode rotational frequency of 1600 rpm; (c) construction of Tafel plots for Pt/ZrP, ZrP@Pt, and Pt/C; (d-e) the Koutecky–Levich (K-L) plots recorded at various potentials for ZrP@Pt and Pt/ZrP; (f) estimation of the H_2O_2 (%) formed and the number of electrons (n) involved in the ORR process as calculated using the RRDE technique.

Tafel plots (**Figure 6c**) give further insight into the ORR kinetics. The measured Tafel slopes for Pt/ZrP, ZrP@Pt and Pt/C are 78, 79 and 69 mV dec^{-1}, respectively, which point towards almost comparable intrinsic activities of the homemade catalysts with the standard Pt/C catalyst. Since Pt is the active site responsible for ORR in both Pt/ZrP and ZrP@Pt, the electrochemical reduction of oxygen is expected to be facilitated through the desired 4-electron reduction transfer process. However, it is important to confirm that ZrP as a carbon-free substrate is not causing any parasitic reaction such as the undesirable 2-electron reduction process leading to H_2O_2 from oxygen. This has been validated with the help of the Koutecky-Levich (K-L) plots (**Figured 6 d-e)**, which relates the parameter j to the diffusion limiting current density (j_d) and kinetic current density (j_k) (see Experimental section for the related equations). The obtained kinetic current density (j_k) of Pt/C, Pt/ZrP and ZrP@Pt at 0.85 V are 1.801, 1.280 and 0.689 mA cm^{-2}, respectively and the

corresponding mass activity calculated using the j_k values are 0.09, 0.064 and 0.034 mA μg^{-Pt}, respectively (see Supporting Information for the calculation) . The average electron transfer is found to be ~ 4.4 for Pt/ZrP while for ZrP@Pt it was ~ 3.8, confirming the 4-electron pathway for the oxygen reduction process, and this further rules out any major undesirable contributions from the carbon-free substrates through parasitic reactions.

Further, there is a possibility that the 4-electron reduction process can be accompanied by mild contributions from the 2-electron reduction process, leading to H_2O_2 as a by-product. Hence, compared to the RDE analysis, which helps to determine the total number of electrons involved in the reduction process, the rotating ring disk electrode (RRDE) analysis can be utilized as an effective tool for quantifying the traces of H_2O_2 formed in case if the catalyst also contributes towards the 2-electron reduction process (see Experimental section for the related equations). Hence, RRDE analysis has been done on the present samples and the amount of H_2O_2 formed has been quantified at the applied potential of 1.2 V *vs*. RHE by maintaining different applied disk electrode potentials. The comparative plots for the ring potential and the disk potential for ZrP@Pt and Pt/ZrP are given in **Figure S9.** As can be seen from **Figure 6f**, the amounts of H_2O_2 measured are 6.8, 2.0, and 3.8 % for ZrP@Pt, Pt/ZrP, and Pt/C, respectively, while maintaining the electron transfer number (n) between 3.8 and 4.0 for the samples. Thus, the RDE and RRDE studies clearly rule out the possibility of any significant contribution by the present catalysts based on the carbon-free substrate towards the undesirable parasitic reaction.

One of the primary reasons to replace C with ZrP is to ensure long-term electrochemical performance and stability by avoiding the corrosion of the support material. To understand how well Pt/ZrP and ZrP@Pt can survive the corrosive environment of the electrochemical ORR process under acidic conditions, an accelerated durability test (ADT) was conducted under triggered conditions wherein the electrocatalysts were cycled under high overpotentials.

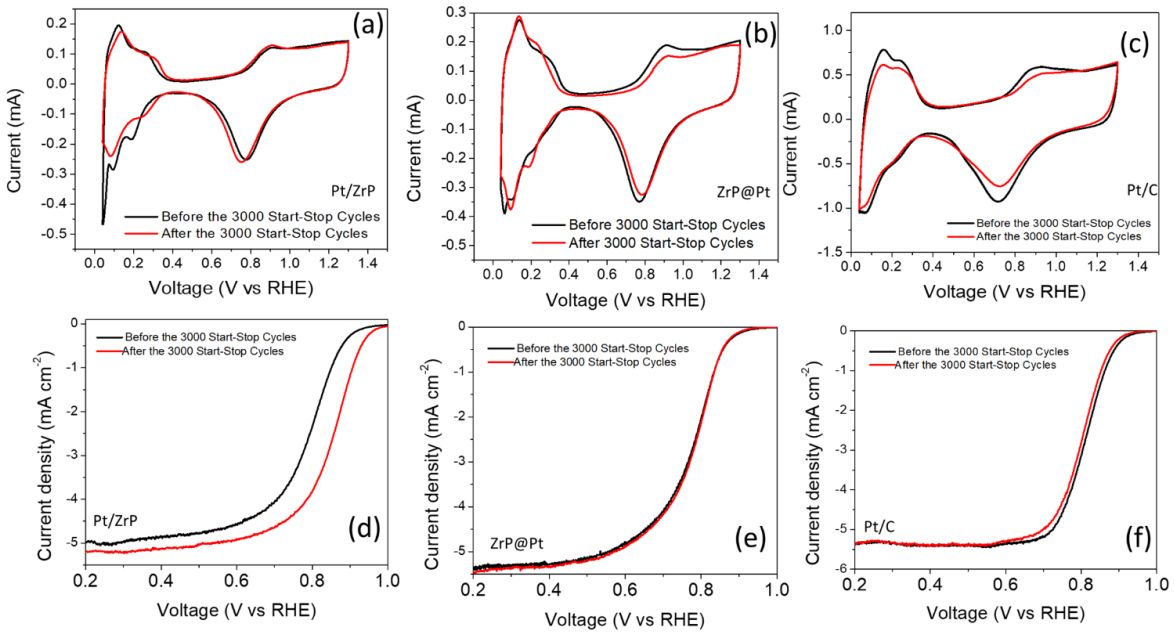

Figure 7. (a-c) The comparative CV profiles recorded for Pt/ZrP, ZrP@Pt, and Pt/C at a scan rate of 50 mV s^{-1} before and after completing the 3000 cycles of ADT, and (d-f) the comparative LSV profiles recorded for Pt/ZrP, ZrP@Pt, and Pt/C before and after completing the 3000 cycles of ADT, recorded at a scan rate of 10 mV s^{-1}.

To study the carbon corrosion, we have done potential cycling between 1.0 V to 1.5 V for 3000 cycles at a scan rate of 100 mV s^{-1} under N_2-saturated electrolyte. These testing conditions are intentionally set to accelerate corrosion of the support material. The complete CV profiles recorded (0.04 V to 1.3 V) before and after the 3000 cycles of ADT (**Figure 7a, 7b** and **7c**) of the homemade catalysts and Pt/C show interesting trends on the changes in the electrochemical properties. While the hydrogen desorption region for both Pt/ZrP and ZrP@Pt display nearly overlapping current-voltage profiles (**Figure 7a** and **7b**), a distinct difference has been observed in the case of the Pt/C catalyst with an estimated drop of 20% from the initial ECSA value (**Figure 7c**). Since the drop in ECSA is directly related to the electrochemical stability of the support material and anchoring strength of the Pt nanoparticles with the substrate, the obtained results clearly point towards the better structural endurance of the ZrP-based catalysts with the Pt nanoparticles strongly adhered to the substrate surface.

To identify the changes brought about to the ORR attributes, LSV profiles were additionally recorded before and after the 3000 cycles of ADT; the corresponding LSV profiles are presented in **Figure 7d, 7e,** and **7f**. The LSV profile corresponding to Pt/ZrP is shown in **Figure 7d**. Pt/ZrP

displays an interesting positive shift in the $E_{1/2}$ by 50 mV subsequent to ADT, which not only highlights the better structural endurance of the catalyst but the trend also hints towards the possible additional favourable structural modulations achieved on the system to further activate the ORR sites (**Figure 7d**). A concomitant improvement in the limiting current density also has been observed in the case of Pt/ZrP subsequent to ADT, possibility due to the potential induced restructuring of the Pt nanoparticles, leading to better exposure of the active sites. In contrast, the LSV profiles corresponding to ZrP@Pt shown in **Figure 7e** do not indicate any ADT induced performance loss and the LSVs recorded before and after the tests are found to be clearly overlapping. However, a negative shift of 10 mV in $E_{1/2}$ has been observed in the case of Pt/C (**Figure 7f**), a trend which is normally observed in the case of the carbon-based catalysts due to the substrate corrosion.

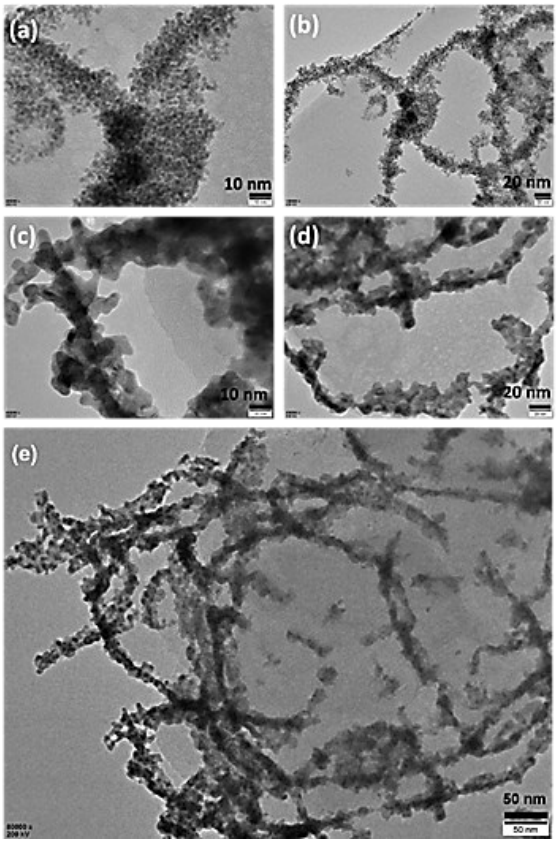

Figure 8. The TEM images of Pt/ZrP recorded to understand the possible changes incurred on the growth pattern of the Pt nanoparticles under the potential induced ORR conditions: (a-b) Pt/ZrP before the 3000 start-stop cycles, and (c-e) Pt/ZrP after the 3000 start-stop cycles.

Also, the mass activity calculated in the case of ZrP@Pt at 0.85 V using the j_k values before and after 3000 cycles of ADT is fund to be unaffected and thus validates the good structural endurance possessed by the system. On the other hand, in the case of Pt/C, the mass activity is

found to be decreased by almost 1.3 times to 0.065 mA μg^{-Pt} whereas, in the case Pt/ZrP, there has been a noticeable increase in the mass activity by 4.6 times to 0.293 mA μg^{-Pt} (refer Supporting Information for the mass activity calculations). This kind of anomalous behaviour was also observed with Pt deposited on the thiolated carbon nanotubes.[37] This can be explained by possible changes in the Pt morphologies or alterations in their growth patterns under the potential induced conditions, with concomitant growth in the particle size leading to a lower ECSA value but optimum particle size, which enhances the ORR activity. A similar type of behavior has been reported on Pt/TaOx/GC (TaOx: amorphous tantalum oxide, GC: glassy carbon), in which the ECSA value was found to be decreasing by almost 43 % with a concomitant increase in the mass activity from 0.20 to 0.32 A $gm^{-Pt}$and the $E_{1/2}$ shift positively by 15 mV.[38] Similarly, Pt-Ni wire which transformed into the branched nanostructure during the potential cycling, and the mass activity was found to be increased from 0.15 A mg^{-Pt} to 0.22 A mg^{-Pt} after 25K cycles.[39] We have carried out the TEM analysis of the ZrP@Pt after ADT, and the structure is found to be stable after 3000 start-stop cycles, as shown in **Figure S10**. The stability can be explained by the strong interaction between the phosphate group and the Pt nanoparticles.

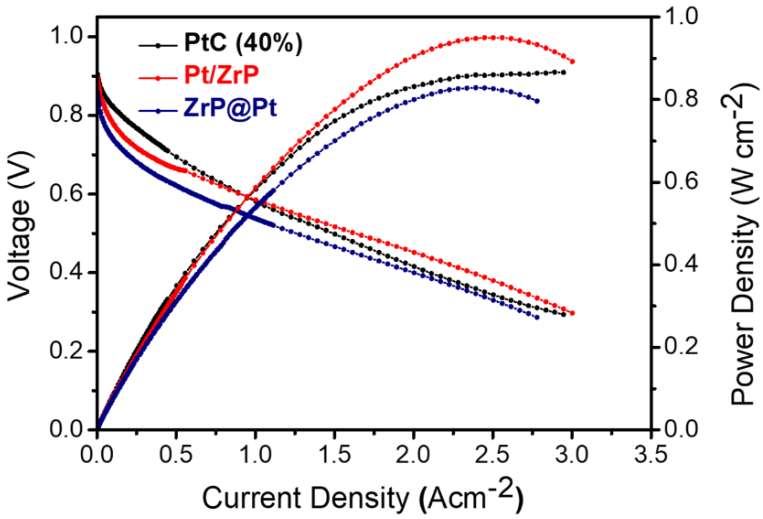

Figure 9. The I-V polarisation plots recorded in the single-cell mode of PEMFC using the membrane electrode assemblies consisting of ZrP@Pt, Pt/ZrP and Pt/C as the electrocatalysts under H_2/O_2 feed condition

As already mentioned, the potential induced activity modulation of Pt/ZrP is pointing towards the possibility of rearrangements of the growth patterns of the Pt nanoparticles. To validate this possibility, post-analysis of the spent Pt/ZrP catalyst was performed by inspecting the nature of the Pt particles with the help of TEM imaging. Accordingly, the TEM data presented in **Figure**

8a-d clearly shows the transformation of the interconnected Pt nanoparticles in the pristine sample (**Figure 8a-b**) into an array of connected nanowires having rough protruded surfaces (**Figure 8c-d)**. The rough surface is known to contain the higher-index facets which are expected to have enhanced ORR activity.[40] This structural transformation might be caused due to the strong interaction between the ZrP and Pt nanoparticles which does not allow the particle to agglomerate and thus restricts the closely distributed nanoparticles of Pt to further interconnect and rearrange the growth pattern .[21] The controlled interplay between the strong interaction between the Pt nanoparticles and phosphate groups, and the close proximity of the interconnected nature of the spherically shaped Pt nanoparticles facilitates this transformation under the potential induced triggered conditions. Ultimately, this structural modulation of the region covering the Pt active sites works in favour of the system to further improve the ORR performance under the potential induced conditions as evident in **Figure 8d**. Furthermore, **Figure 8e** clearly shows that the geometry of the ZrP substrate as well as the distribution characteristics of the Pt nanoparticles along the edges of the substrate is intact, thus pointing toward the high stability of Pt/ZrP under the experimental conditions.

The realistic PEMFC test was performed by fabricating the MEAs based on the anode and cathode electrodes made up of the homemade catalysts, along with a standard MEA derived from the Pt/C catalyst. In order to make the electrodes, 0.50 mg/cm^2 of the respective catalysts were brush-coated on the carbon paper-based GDL. The MEAs were subsequently made by sandwiching the anode and cathode electrodes with the Nafion-HP membranes by means of hot-pressing. The single-cell tests were conducted by following the standard testing protocols by maintaining the operating conditions of the cells as 60 % relative humidity (RH) and 70 °C operating temperature, using a test fixture connected to the fuel cell test station. The current (I)-voltage (V) polarisation plots were recorded in the H_2/O_2 feed condition. **Figure 9** represents the I-V polarization plots along with the power density profiles recorded for the Pt/ZrP, ZrP@Pt and Pt/C based MEAs. It is interesting to note that the MEAs based on the homemade catalysts display promising performances and, more specifically, the one based on Pt/ZrP is found to be even outperforming the Pt/C-based MEA at above 0.60 V in terms of the current density and power density. At 0.60 V, which has been treated as the practical operating potential of the normal fuel cell operations, the MEAs based on ZrP@Pt, Pt/ZrP and Pt/C exhibit the current densities of 0.60, 0.891 and 0.890 A cm^{-2}, respectively (**Figure 9**). There is a nice correlation between the results obtained in the single-cell validation and the intrinsic ORR characteristics as mapped through the single-electrode studies. The lower performance obtained with ZrP@Pt compared to Pt/ZrP conforms to the ORR data. The maximum power densities achieved with

ZrP@Pt, Pt/ZrP and Pt/C based MEAs are 0.86, 0.95 and 0.83 W cm^{-2}, respectively. The two notable features of the I-V plot traced by the Pt/ZrP-based MEA, in comparison to that based on Pt/C, are the comparatively high overpotential incurred in the activation polarization region (*i.e*. the low current density region) and the better performance in the mass transfer sensitive region (*i.e*., the high current density region) by the homemade system. Most probably, the iR drop originated by the relatively low conductivity of the carbon-free substrate might have played a dominant role in the activation polarization region, leading to a notable drop in the performance. However, the system soon recovers from this issue when it gains from the advantageous factors like the intrinsic proton conductivity of the substrate, better exposure and accessibility of the Pt particles and overall improved mass transfer characteristics. The single-cell data thus points towards the better prospects of Pt/ZrP as a viable carbon-free alternative to the state-of-the-art catalysts without compromising the performance requirements.

We have kept the different catalysts for ten days of aging at a pH of 5.[41] At 60 % humidity, regardless of the temperature, the fuel cell shows a pH of around 5.[41] We have done the HR-TEM analysis and EDS after ten days. In the case of Pt/ZrP and ZrP@Pt, the structure remains stable compared to that of Pt/C. **Figure S11** shows that Pt/ZrP and ZrP@Pt before and after ten days of aging at a pH of 5 clearly show that the ZrP structure and the Pt dispersion characteristics are intact. Further, EDS mapping has been carried out, confirming the presence of the Zr, O, P, and Pt in ZrP@Pt and Pt/ZrP. Also, the HAADF-STEM images show the presence of Pt along the edges and on the surface in Pt/ZrP and ZrP@Pt, respectively (**Figure S12**).

3. Conclusion

In summary, a new class of carbon-free electrocatalysts for oxygen reduction reaction (ORR) has been created by decorating Pt nanoparticles on zirconium phosphate (ZrP) nanoplates, which display solid-state proton conductivity. Two distinct types of dispersion patterns of the nanoparticles of Pt (4o wt.%) on ZrP nanoplates have been observed. In the first case, represented as ZrP@Pt, the Pt nanoparticles are found to be closely distributed and completely covering the ZrP nanoplates, whereas, in the second case, designated as Pt/ZrP, the Pt nanoparticles have selectively restricted dispersion along the edges of the support. The proton conductivity of ZrP nanoplates ranges from 0.26 x 10^{-4} S cm^{-1} to 0.50 x 10^{-4} S cm^{-1} at 40 to 70 ^{o}C in 95 % humidity with an activation energy (E_a) of 0.19 eV. Both ZrP@Pt and Pt/ZrP are displaying promising ORR characteristics. However, Pt/ZrP is found to be an interesting system with respect to its ORR performance because the system shows enhancement in the

performance during the course of the electrochemical potential cycling processes. This favourable activity modulation towards ORR is found to be originated from the transformation of the interconnected Pt nanoparticles along the edges of ZrP into an array of connected nanowires having rough protruded surfaces. This results in the increase of the roughness factor and exposure of the higher-index facets, thus contributing favourably towards ORR. Also, the composite catalyst shows strong evidence of charge transfer from the ZrP to the Pt nanoparticles, leading to strong metal-support interactions. The strong anchoring of the Pt with the phosphate group is possibly the reason for the observed high durability of the ZrP-based catalysts. Also, the observed more positive onset potential and $E_{1/2}$ values of Pt/ZrP compared to ZrP@Pt can be attributed to strong electronic interaction between ZrP and Pt as validated through the XPS results, which can directly affect the strength of adsorption of the oxygen and oxygen intermediates. The single-cell evaluation of the MEAs based on Pt/ZrP and ZrP@Pt displayed a trend that conforms to the intrinsic ORR performance of the systems. The performance of the MEA based on Pt/ZrP is found to be superior to that of the one based on Pt/C at the operating potentials above 0.60 V. The controlled interplay of the advantageous factors such as the activation induced morphological transformation of the dispersed state of the Pt nanoparticles, intrinsic proton conductivity of the ZrP substrate, better exposure and accessibility of the Pt nanoparticles and overall improved mass transfer characteristics of the catalyst layer are expected to be favouring the cell based on the homemade catalyst. Thus, Pt/ZrP is found to be a versatile and potential replacement for the state-of-the-art catalysts with distinct prospects for minimizing the issues related to the carbon-corrosion.

4. Experimental

4.1. Synthetic Procedures: Synthesis of the zirconium phosphate (ZrP) nanoplates: In a typical synthesis route of ZrP, 1.4 g of zirconium oxynitrate was added into the 20 ml of 6.0 M H_3PO_4 in a 25 ml autoclave. The mixture was subsequently solubilised for 5 min. and was kept at 200 ^oC for 4 h. The product was obtained by centrifugation at 8000 rpm for 5 min. and was washed with DI water until the pH of the supernatant becomes equal to the pH of the DI water. The obtained product was dried for 12 h at 60 ^oC.

4.2. ZrP nanoplates encapsulated with 40 wt.% Pt nanoparticles (ZrP@Pt): 60 mg of the ZrP was first dispersed in water by sonication; followed by this, the required amount of $H_2PtCl_6.6H_2O$ was added based on a targeted Pt loading of 40 wt.%. After sonication for 5 min., ethylene glycol was added into the above suspension and again the mixture was sonicated for 30 min. Followed by the addition of urea into the above mixture, the suspension was stirred for

10-12 h at 35 ^{o}C and thereafter heated at 120 ^{o}C for 1 h. The wet cake obtained after filtration was washed sequentially with water and ethanol. The obtained product was kept for drying at 70 ^{o}C for 10-12 h. The product thus obtained is designated as ZrP@Pt since the Pt nanoparticles are found to be covering the entire surface of the ZrP nanoplates.

4.3. ZrP nanoflakes bearing 40 % Pt nanoparticles along the edges (Pt/ZrP): The synthesis procedure involved in this case was similar to that of ZrP@Pt except for the ageing of the ZrP which was carried out by stirring the suspension for 24 h after adding ethylene glycol, compared to 12 h as performed in the previous case. The product thus obtained is designated as Pt/ZrP since the Pt nanoparticles are found to be dispersed selectively along the edges of the nanoplates of ZrP.

4.4. Physical Characterization: Field emission scanning electron microscopy (performed on FEI Nova Nano SEM 450) and transmission electron microscopy (carried out on FEI TECNAI G2F20 instrument) were employed to gain information related to the morphological features of the prepared materials. A Quanta 2003D FEI instrument in combination with a TEAM TM EDS analysis system was used for performing the energy-dispersive X-ray spectroscopy (EDS) elemental mapping and a JEM-F200 instrument was used for performing the HAADF-STEM analysis. For examining the electronic properties of the different catalysts, X-ray photoelectron spectroscopy (XPS) was performed on the Thermo Scientific K-Alpha + machine with a fully integrated monochromated small-spot X-ray photoelectron spectrometer (XPS) system.

4.5. Electrochemical Characterization: For the electrochemical characterization, 20 µl of the catalyst slurry of Pt/ZrP or ZrP@Pt (prepared by dispersing 5 mg of the respective catalyst in 1.0 ml ethanol and 1.0 ml of DI water by sonication) was drop-coated on the glassy carbon rotating disc electrode (RDE) (geometric area of 0.196 cm^2). The electrode was subsequently dried under an IR lamp. In the case of the electrode preparation with the Pt/C (40 %) catalyst for control studies, the slurry was prepared by sonicating 5 mg of the catalyst in a mixture of 0.75 ml of DI water and 0.25 ml of isopropyl alcohol (IPA) along with 40 µl of 5 wt. % Nafion as a binder. 10 µl of the slurry was drop-coated on the glassy carbon electrode, followed by drying the coating under an IR lamp. All the RDE experiments were conducted in fresh 0.1 M $HClO_4$ solution using Ag/AgCl as the reference electrode (RE), and a graphite rod as a counter electrode. The measurements were performed on a Biologic potentiostat (SP-300) combined with a Pine RDE unit. Rotating ring disk electrode (RRDE) system was used to determine the amount of H_2O_2 produced and the number of electrons transferred during the oxygen reduction

process. The equations used for quantifying the H_2O_2 % and the electron transfer number (n) are as follows:

$$\boldsymbol{H_2O_2}(\%) = (\boldsymbol{200 i_r/N})/(\boldsymbol{\frac{i_r}{N} + i_d}); \boldsymbol{n = 4 i_d/ (i_d + \frac{i_r}{N})}$$

where, i_d and i_r are the disks and the ring currents and N is the current collection efficiency.[42] The measurements were performed by keeping the ring at a potential of 1.2 V *vs*. RHE. Further, Kountechy-Levich (K-L) plots were constructed from the LSV profiles recorded through the rotating disc electrode (RDE) mode, and based on the kinetic current density (j_k) measured at 0.85 V, the mass activity of the catalysts for oxygen reduction was calculated. The mass activity was calculated using j_k and by normalizing with respect to the mass of the active components (Pt) in the system. The kinetic current density was calculated using the K-L equation:

$$\frac{1}{j} = \frac{1}{jd} + \frac{1}{jk}$$

This equation was used for constructing the K-L plots by plotting the inverse of the current density ($1/j$) and angular frequency of rotation ($\omega^{-1/2}$), where, j is the observed current density, j_d is the limiting current density, and j_k is the kinetic current density.[43] Here, $j_d = 0.62nFAD^{2/3}v^{-1/6}\omega^{1/2}C_{O2}$, where, n is the number of electrons transferred, F is Faraday's constant (96 500 C), v is the kinematic viscosity of the electrolyte, ω is the angular frequency of rotation, D is the diffusion coefficient of O_2 in 0.1 M $HClO_4$, A is the electrode area (0.196 cm^2), and C_{O2} is the concentration of molecular oxygen in the electrolyte in 0.1 M $HClO_4$. Carbon corrosion measurement was done by performing 3000 cycles of potential scanning under nitrogen-enriched conditions in the range of ~ 1.0 to 1.5 V (scan rate: 100 mV s^{-1}) and comparing the results before in fresh 0.1 M $HClO_4$ and after the 3000 cycles in fresh 0.1 M $HClO_4$.

4.6. Proton Conductivity measurement: Proton conductivity of the material was measured using electrochemical impedance spectroscopy (EIS) in humidified conditions. For the measurements, a homemade setup was used, where the pellets of the material (13 mm in diameter) were placed between two stainless steel electrodes and the set-up was moved inside a humidity-controlled temperature chamber (SH-241, ESPEC Co. Ltd., Japan), which was also connected to an electrochemical workstation (VMP-3) from BioLogic. The sample was left inside the humidity chamber for at least 1 h for equilibration before the measurements. For the EIS measurements, an input AC voltage of amplitude of 10 mV was applied to the pellet under OCV conditions and the frequency was scanned from 1 MHz and 0.1 Hz. In each case, the proton conductivity was calculated using the Pouillet's equation, $\sigma = L/R \times A$, where, σ is the

conductivity (S cm^{-1}), L is the thickness of the measured sample (cm) and A is the electrode area (in cm^{-2}).[44]

4.7. Single-cell testing of PEMFC: In the present study, DuPont™ Nafion® HP membranes was used as the proton conducting membrane. The electrode slurry for both the anode and cathode electrodes was prepared by mixing Pt/ZrP, functionalized carbon and Nafion-20 wt% (DuPont, USA) in isopropanol using bath sonication for 2 h. In the case of Pt/ZrP, the ionomer to catalyst ratio was maintained at 0.30. The electrode was prepared by applying the slurry to a gas diffusion layer (GDL) (SGL Carbon Company) with an anode and cathode Pt loading of 0.50 mg cm^{-2}. The electrodes (3.5 cm x 3.5 cm in size) were vacuum dried at 130 °C and hot pressed at 130 ºC against the Nafion™ HP membrane for 3 min. to prepare the MEA. Subsequently, the MEA was fixed in a standard test fixture (Fuel Cell Technologies, Inc., USA) by applying a torque of 3 Nm. Hydrogen was used as the fuel and oxygen/air gas were used as the oxidant. The testing was performed at 70 ºC with a relative humidity of 60 %.

Supporting Information

Supporting Information is available from the Wiley Online Library or from the author.

Acknowledgements

S. Kumar acknowledges the University Grant Commission (UGC), New Delhi, India, for a Senior Research Fellowship. S. Kurungot acknowledges the Council of Scientific and Industrial Research (CSIR), New Delhi, India, for the funding of the project through NCP-Energy (MLP102226).

Received: ((will be filled in by the editorial staff))
Revised: ((will be filled in by the editorial staff))
Published online: ((will be filled in by the editorial staff))

References

[1] L. Wang, W. Gao, Z. Liu, Z. Zeng, Y. Liu, M. Giroux, M. Chi, G. Wang, J. Greeley, X. Pan, C. Wang, *ACS Catal.* **2018**, *8*, 35.

[2] W. J. Lee, J. S. Lee, H. Y. Park, H. S. Park, S. Y. Lee, K. H. Song, H. J. Kim, *Int. J. Hydrogen Energy* **2020**, *45*, 32825.

[3] G. S. Avcioglu, B. Ficicilar, I. Eroglu, *Int. J. Hydrogen Energy* **2016**, *41*, 10010.

[4] J. Parrondo, T. Han, E. Niangar, C. Wang, N. Dale, K. Adjemian, V. Ramani, *Proc. Natl. Acad. Sci. U. S. A.* **2014**, *111*, 45.

[5] S. Ott, A. Orfanidi, H. Schmies, B. Anke, H. N. Nong, J. Hübner, U. Gernert, M. Gliech, M. Lerch, P. Strasser, *Nat. Mater.* **2020**, *19*, 77.

[6] S. Liu, K. Wippermann, W. Lehnert, *Int. J. Hydrogen Energy* **2021**, *46*, 14687.

[7] L. Chong, J. Wen, J. Kubal, F. G. Sen, J. Zou, J. Greeley, M. Chan, H. Barkholtz, W. Ding, D. J. Liu, *Science (80-.).* **2018**, *362*, 1276.

[8] C. Lafforgue, F. Maillard, V. Martin, L. Dubau, M. Chatenet, *ACS Catal.* **2019**, 5613.

[9] H. S. Oh, J. H. Lee, H. Kim, "Electrochemical carbon corrosion in high temperature proton exchange membrane fuel cells," **2012**.

[10] L. Castanheira, W. O. Silva, F. H. B. Lima, A. Crisci, L. Dubau, F. Maillard, *ACS Catal.* **2015**, *5*, 2184.

[11] N. N. Krishnan, S. Lee, R. V. Ghorpade, A. Konovalova, J. H. Jang, H. J. Kim, J. Han, D. Henkensmeier, H. Han, *J. Memb. Sci.* **2018**, *560*, 11.

[12] V. Kurdakova, E. Quartarone, P. Mustarelli, P. Magistris, E. Caponetti, M. L. Saladino, *J. Power Sources* **2010**, *195*, 7765.

[13] Y. Devrim, H. Devrim, I. Eroglu, *Int. J. Hydrogen Energy* **2016**, *41*, 10044.

[14] F. J. Pinar, P. Cañizares, M. A. Rodrigo, D. Ubeda, J. Lobato, *RSC Adv.* **2012**, *2*, 1547.

[15] M. Pica, R. Vivani, A. Donnadio, E. Troni, S. Fop, M. Casciola, *Inorg. Chem.* **2015**, *54*, 9146.

[16] A. Ozden, M. Ercelik, Y. Ozdemir, Y. Devrim, C. O. Colpan, *Int. J. Hydrogen Energy* **2017**, *42*, 21501.

[17] A. K. Sahu, S. Pitchumani, P. Sridhar, A. K. Shukla, *Fuel Cells* **2009**, *9*, 139.

[18] A. Al-Othman, A. Y. Tremblay, W. Pell, S. Letaief, T. J. Burchell, B. A. Peppley, M. Ternan, *J. Power Sources* **2010**, *195*, 2520.

[19] O. Barron, H. Su, V. Linkov, B. G. Pollet, S. Pasupathi, *J. Power Sources* **2015**, *278*, 718.

[20] H. Mohammed, A. Al-Othman, P. Nancarrow, Y. Elsayed, M. Tawalbeh, *Int. J. Hydrogen Energy* **2021**, *46*, 4857.

[21] K. S. Lee, S. J. Yoo, D. Ahn, S. K. Kim, S. J. Hwang, Y. E. Sung, H. J. Kim, E. Cho, D. Henkensmeier, T. H. Lim, J. H. Jang, "Phosphate adsorption and its effect on oxygen reduction reaction for PtxCoy alloy and Aucore-Ptshell electrocatalysts," **2011**.

[22] X. Zhang, J. Shen, S. Pan, J. Qian, B. Pan, *Adv. Funct. Mater.* **2020**, *30*, 1909014.

[23] H. Yano, T. Akiyama, P. Bele, H. Uchida, M. Watanabe, *Phys. Chem. Chem. Phys.* **2010**, *12*, 3806.

[24] D. M. Kaschak, S. A. Johnson, D. E. Hooks, H. Kim, M. D. Ward, T. E. Mallouk, *J. Am. Chem. Soc.* **1998**, *120*, 10887.

[25] C. Cui, L. Gan, H. H. Li, S. H. Yu, M. Heggen, P. Strasser, *Nano Lett.* **2012**, *12*, 5885.

[26] T. Tamaki, H. Kuroki, S. Ogura, T. Fuchigami, Y. Kitamoto, T. Yamaguchi, *Energy Environ. Sci.* **2015**, *8*, 3545.

[27] M. C. Tsai, T. T. Nguyen, N. G. Akalework, C. J. Pan, J. Rick, Y. F. Liao, W. N. Su, B. J. Hwang, *ACS Catal.* **2016**, *6*, 6551.

[28] S. Kumar, S. N. Bhange, R. Soni, S. Kurungot, *ACS Appl. Energy Mater.* **2020**, *3*, 1908.

[29] J. L. Colón, D. S. Thakur, C. Y. Yang, A. Clearfield, C. R. Martini, *J. Catal.* **1990**, *124*, 148.

[30] I. Jiménez-Morales, S. Cavaliere, D. Jones, J. Rozière, *Phys. Chem. Chem. Phys.* **2018**, *20*, 8765.

[31] M. Y. Smirnov, A. V. Kalinkin, E. I. Vovk, P. A. Simonov, E. Y. Gerasimov, A. M. Sorokin, V. I. Bukhtiyarov, *Appl. Surf. Sci.* **2018**, *428*, 972.

[32] B. J. Hsieh, M. C. Tsai, C. J. Pan, W. N. Su, J. Rick, J. F. Lee, Y. W. Yang, B. J. Hwang, *NPG Asia Mater.* **2017**, *9*, DOI 10.1038/am.2017.78.

[33] G. Zhang, Z. Yang, W. Zhang, Y. Wang, *J. Mater. Chem. A* **2017**, *5*, 1481.

[34] A. Kumar, V. Ramani, *ACS Catal.* **2014**, *4*, 1516.

[35] G. Xing, T. Yan, S. Das, T. Ben, S. Qiu, *Angew. Chemie* **2018**, *130*, 5443.

[36] T. Bayer, B. V. Cunning, R. Selyanchyn, M. Nishihara, S. Fujikawa, K. Sasaki, S. M. Lyth, *Chem. Mater.* **2016**, *28*, 4805.

[37] T. J. Kim, G. Kwon, Y. T. Kim, *Chem. Commun.* **2014**, *50*, 596.

[38] Z. Awaludin, J. G. Sheng Moo, T. Okajima, T. Ohsaka, *J. Mater. Chem. A* **2013**, *1*, 14754.

[39] M. Kato, Y. Iguchi, T. Li, Y. Kato, Y. Zhuang, K. Higashi, T. Uruga, T. Saida, K. Miyabayashi, I. Yagi, *ACS Catal.* **2022**, *12*, 259.

[40] L. Bu, S. Guo, X. Zhang, X. Shen, D. Su, G. Lu, X. Zhu, J. Yao, J. Guo, X. Huang, *Nat. Commun.* **2016**, *7*, 11850.

[41] A. M. Abdullah, T. Okajima, F. Kitamura, T. Ohsaka, *ECS Trans.* **2008**, *16*, 543.

[42] L. Wang, Z. Tang, W. Yan, H. Yang, Q. Wang, S. Chen, *ACS Appl. Mater. Interfaces* **2016**, *8*, 20635.

[43] D. Wang, H. L. Xin, R. Hovden, H. Wang, Y. Yu, D. A. Muller, F. J. Disalvo, H. D. Abruña, *Nat. Mater.* **2013**, *12*, 81.

[44] K. C. Ranjeesh, R. Illathvalappil, S. D. Veer, J. Peter, V. C. Wakchaure, Goudappagouda, K. V. Raj, S. Kurungot, S. S. Babu, *J. Am. Chem. Soc.* **2019**, *141*, 14950.

Supporting Information

Pt-Anchored-Zirconium Phosphate Nanoplates as High-Durable Carbon-free Oxygen Reduction Reaction Electrocatalyst for PEM Fuel Cell Applications

Sachin Kumar,[a, b, ‡] *Athira Yoyakki,*[a, ‡] *Ajmal Pandikassala,*[a,b] *Roby Soni,*[c] *and Sreekumar Kurungout*[a,b,*]

[a] Physical and Materials Chemistry Division, CSIR-National Chemical Laboratory, Dr Homi Bhabha Road, Pune 411 008, India. E-mail: k.sreekumar@ncl.res.in

[b] Academy of Scientific and Innovative Research, Ghaziabad, 201002, India

[c] Electrochemical Innovation Laboratory, Department of Chemical Engineering, University College London, Gower Street, London, WC1E 6BT, UK

‡ Both authors contribute equally

E-mail: k.sreekumar@ncl.res.in

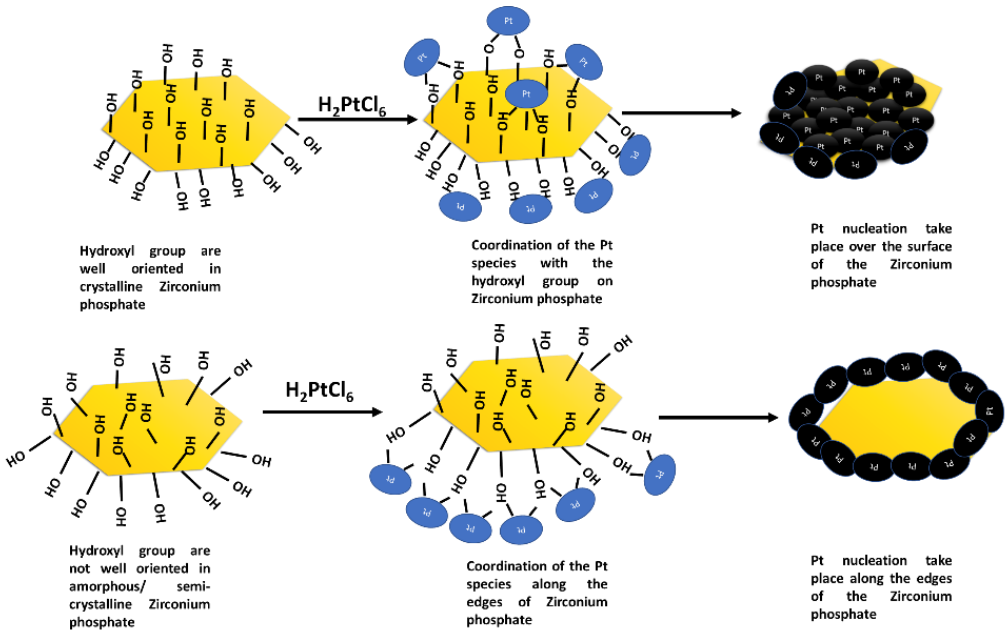

Figure S1 The proposed mechanism of the Pt nanoparticle-decoration along the surface (ZrP@Pt) and edges (Pt/ZrP) of ZrP.

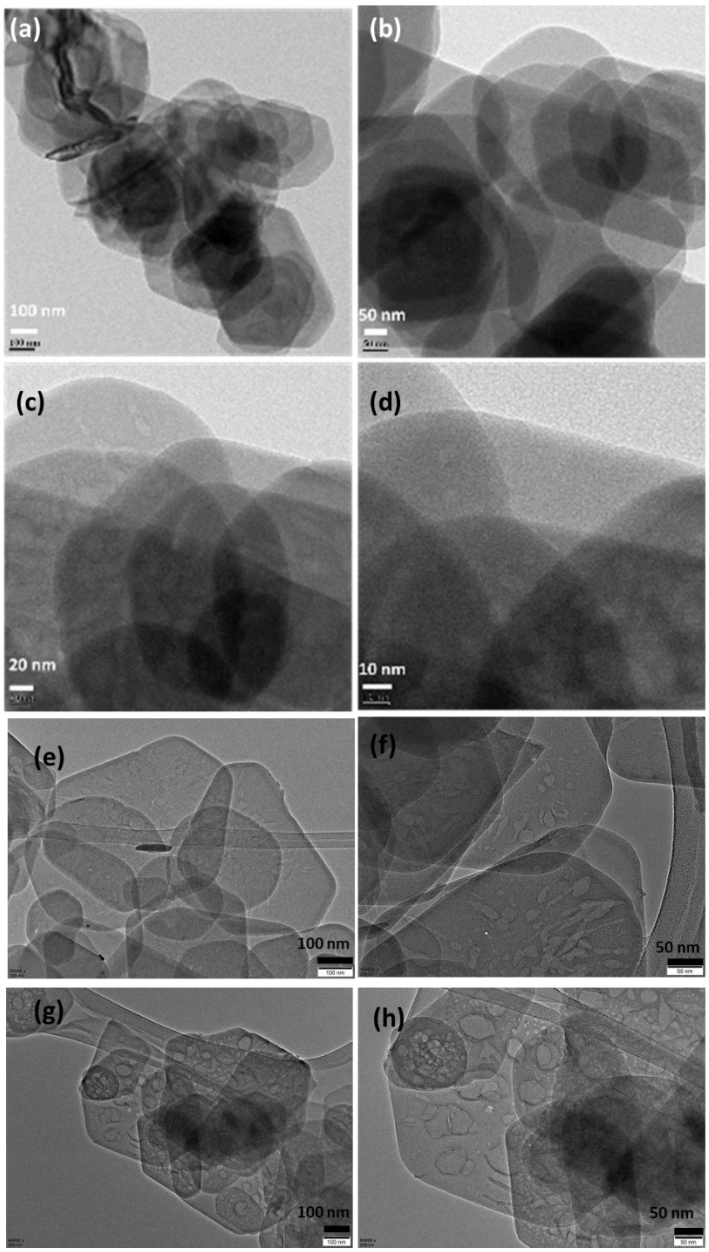

Figure S2. The TEM images of the as-synthesized (a-d) ZrP nanoplates, recorded at various magnifications and (e-f) shows the ZrP plates aged at 12 and 24 hrs.

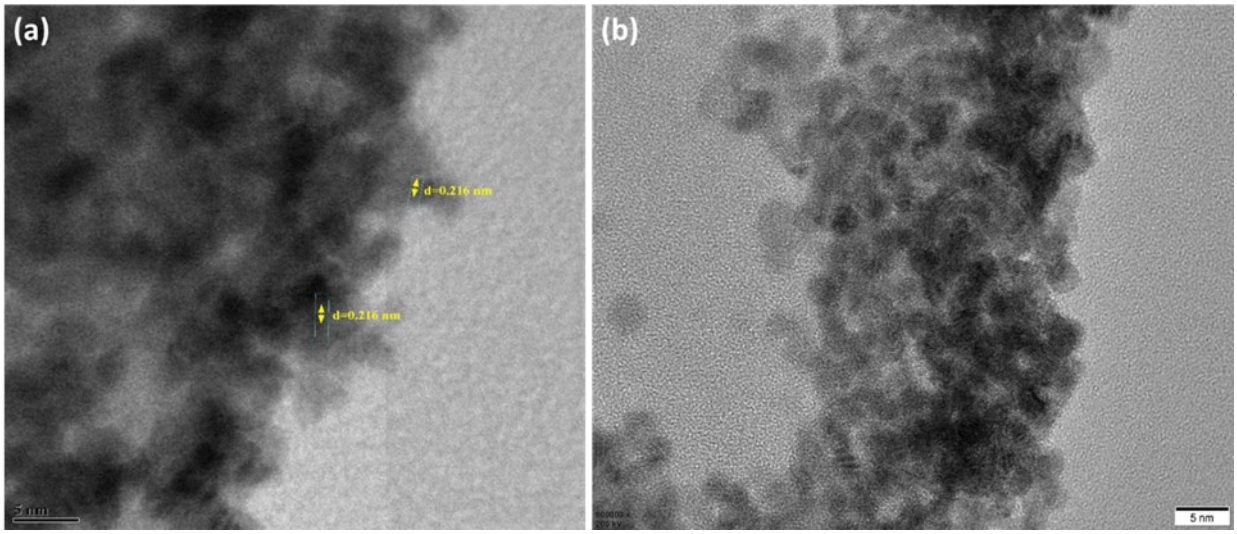

Figure S3. The HR-TEM images of (a) ZrP@Pt, and (b) Pt/ZrP.

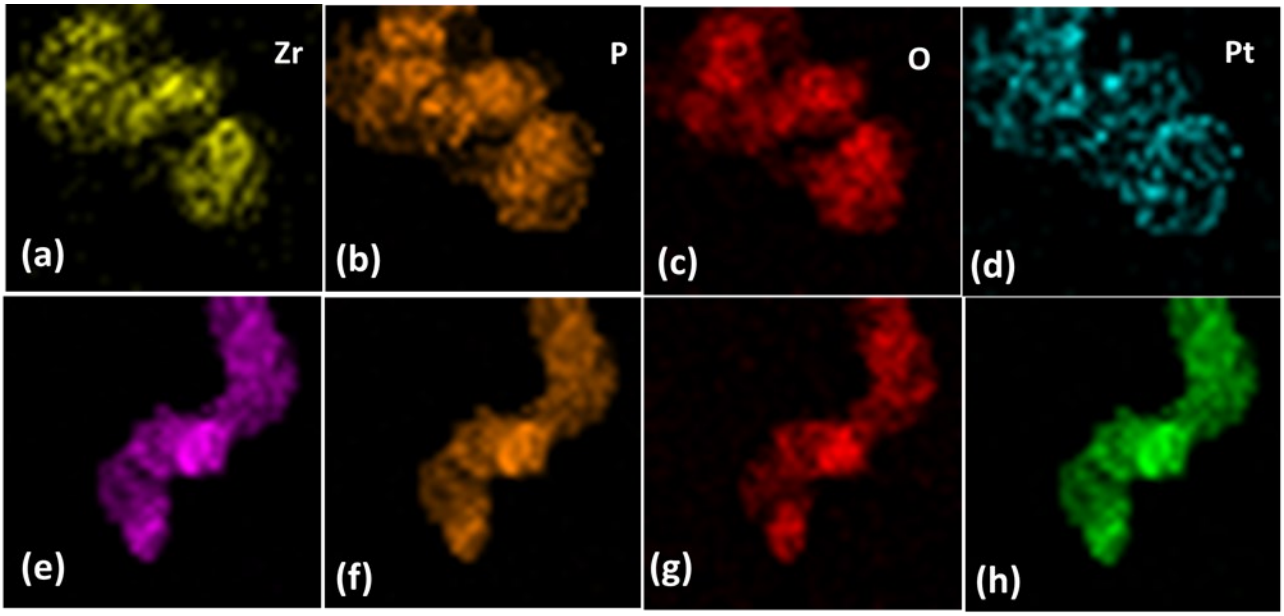

Figure S4. EDS mapping of Pt/ZrP (a-d), and ZrP@Pt (e-h) showing the various elements, *viz*., Pt, Zr, O and P, preset in the system.

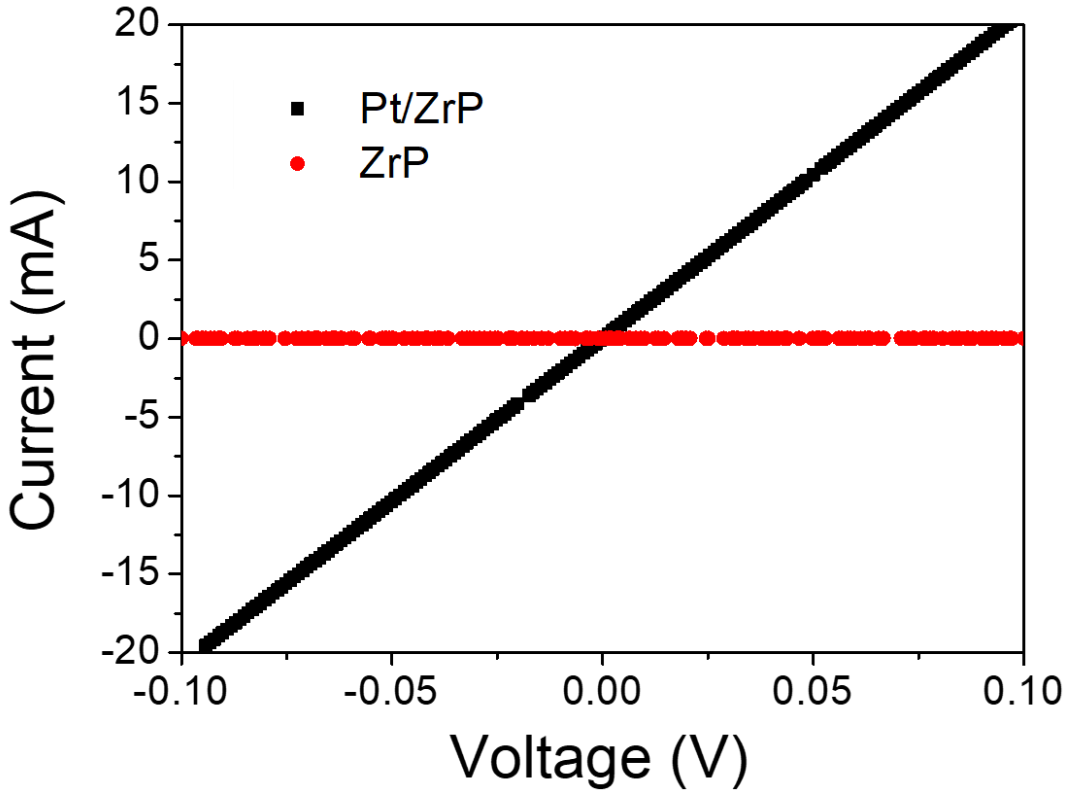

Figure S5. The I-V polarisation plots recorded for ZrP and Pt/ZrP to investigate the electronic conductivity characteristics of the materials.

Samples	Electronic conductivity
ZrP	6.8 x 10^{-3} S m^{-1}
Pt/ZrP	8.5 S cm^{-1}
ZrP@Pt	~1 S cm^{-1}
Carbon	47 S cm^{-1}
Pt/C	18 S cm^{-1}

Table S1. Showing the electronic conductivity value of the different samples.

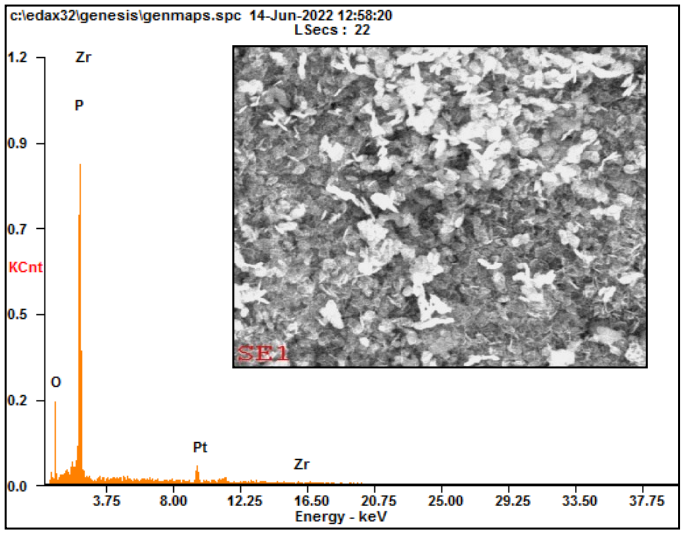

	Wt%	At%
OK	25.96	65.60
PK	10.58	13.81
ZrL	31.51	13.97
PtL	31.95	06.62
Matrix	Correction	ZAF

Figure S6. EDS spectra of Pt/ZrP showing the wt. % of different element.

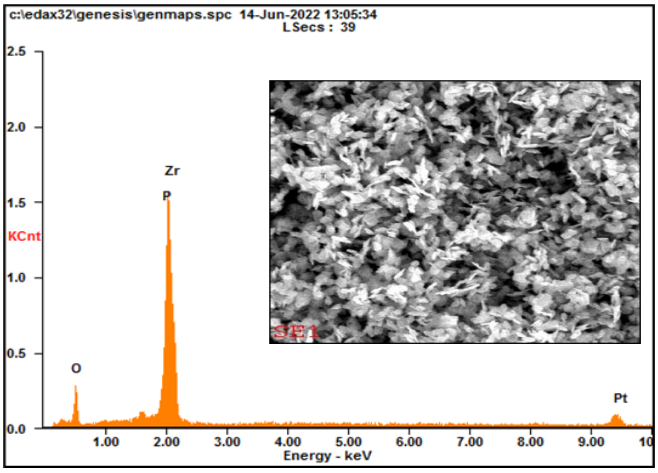

Element	Wt%	At%
OK	21.64	61.18
PK	09.60	14.03
ZrL	33.52	16.62
PtL	35.24	08.17
Matrix	Correction	ZAF

Figure S7. EDS spectra of ZrP@Pt showing the wt. % of different element.

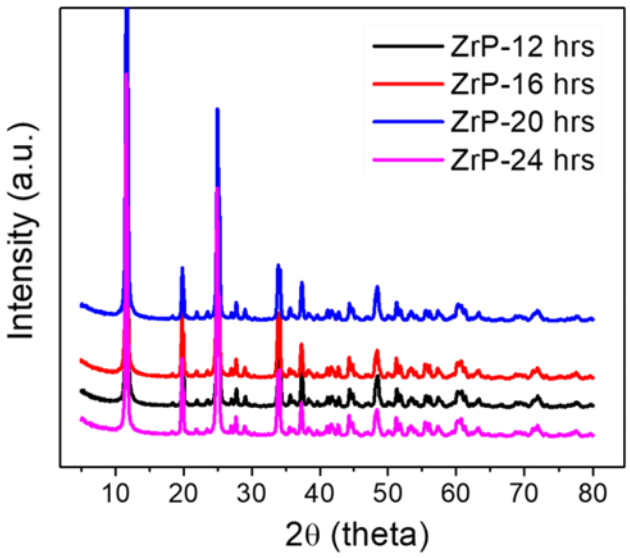

Figure S8. The XRD analysis carried out for the ZrP aged at different time periods.

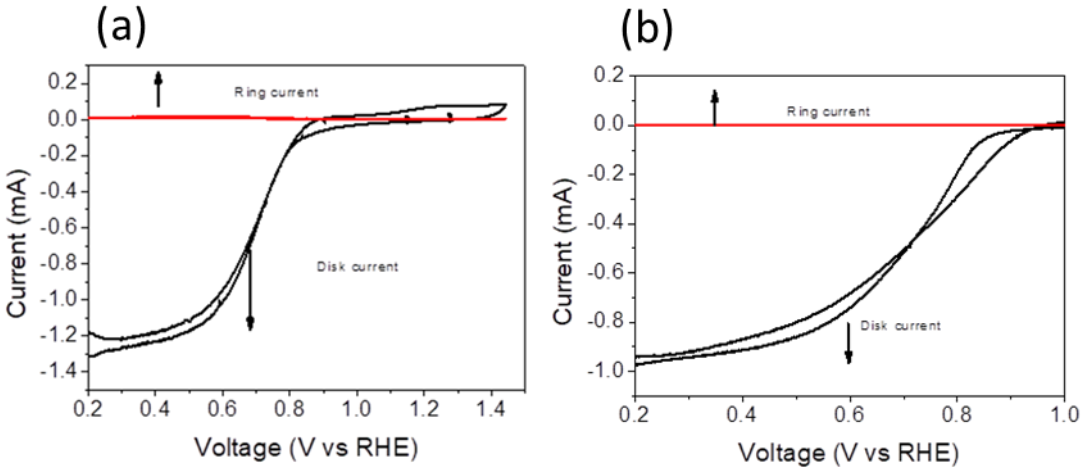

Figure. S9. The RRDE plots showing the ring current and disk current during the ORR experiment with ZrP@Pt (a), and Pt/ZrP (b).

Calculation of the proton conductivity:

The proton conductivity was calculated using the Pouillet's equation:

$$\sigma = L/(R \times A),$$

where, L is the thickness of the measured sample (cm), σ is the conductivity (S cm^{-1}) and A is the electrode area (in cm^{-2}).

L = 0.108 cm; r=0.65 cm; R = 1643.68 Ω

$$\sigma = \frac{0.1080}{3.14\times0.65\times0.65\times1643.68} = 0.495279\times10^{-4}\ \text{S cm}^{-1}$$

Calculation of the mass activity using kinetic current density:

$$\frac{1}{j} = \frac{1}{jd} + \frac{1}{jk}$$

where, J is the observed current density, j_d is the limiting current density, and j_k is the kinetic current density. Here, $j_d = 0.62nFAD^{2/3}v^{-1/6}\omega^{1/2}C_{O2}$, where, n is the number of electrons transferred, F is the Faraday's constant (96 500 C), A is the electrode area (0.196 cm^2), v is the kinematic viscosity of the electrolyte, D is the diffusion coefficient of O_2 in 0.1 M $HClO_4$, ω is the angular frequency of rotation and C_{O2} is the concentration of molecular oxygen in the electrolyte in 0.1 M $HClO_4$.

$$j_k = \frac{j_d \times j}{j_d - j}$$

Mass activity = $\frac{jk}{(\ active\ mass\ of\ Pt\ )}$

$j_{k\_(Pt/C)} = \left| \frac{1.35 \times 5.39}{5.39-1.39} \right|$; Mass activity (@ 0.85 V) = $\frac{1.801\ mA}{20\ \mu g}$ = 0.09 mA μg^{-1}

$j_{k\_(Pt/ZrP)} = \left| \frac{1.02 \times 4.96}{4.96-102} \right|$; Mass activity (@ 0.85 V) = $\frac{1.28\ mA}{20\ \mu g}$ = 0.064 mA μg^{-1}

$j_{k\_(ZrP@Pt)} = \left| \frac{0.61 \times 5.37}{5.37-0.618} \right|$; Mass activity (@ 0.85 V) = $\frac{0.689\ mA}{20\ \mu g}$ = 0.034 mA μg^{-1}

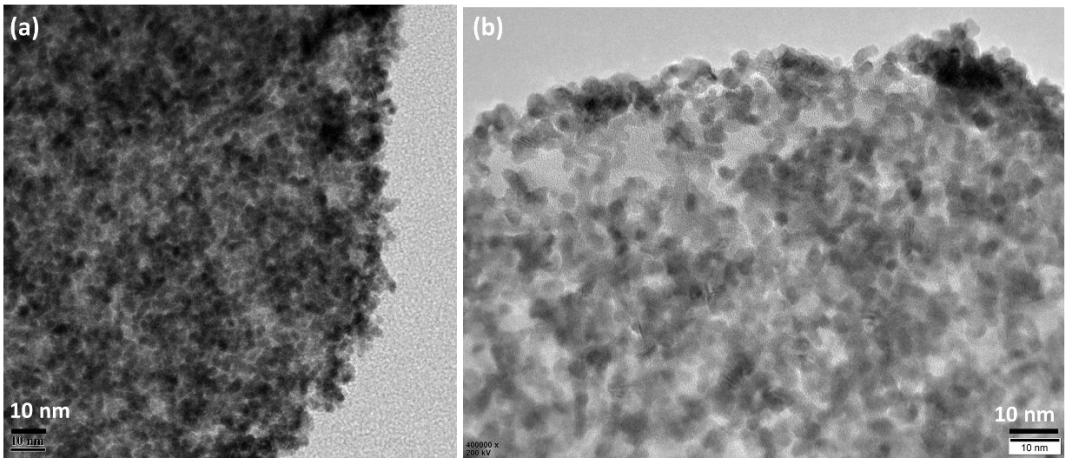

Figure S10. TEM images of ZrP@Pt before and after 3000 cycles of ADT.

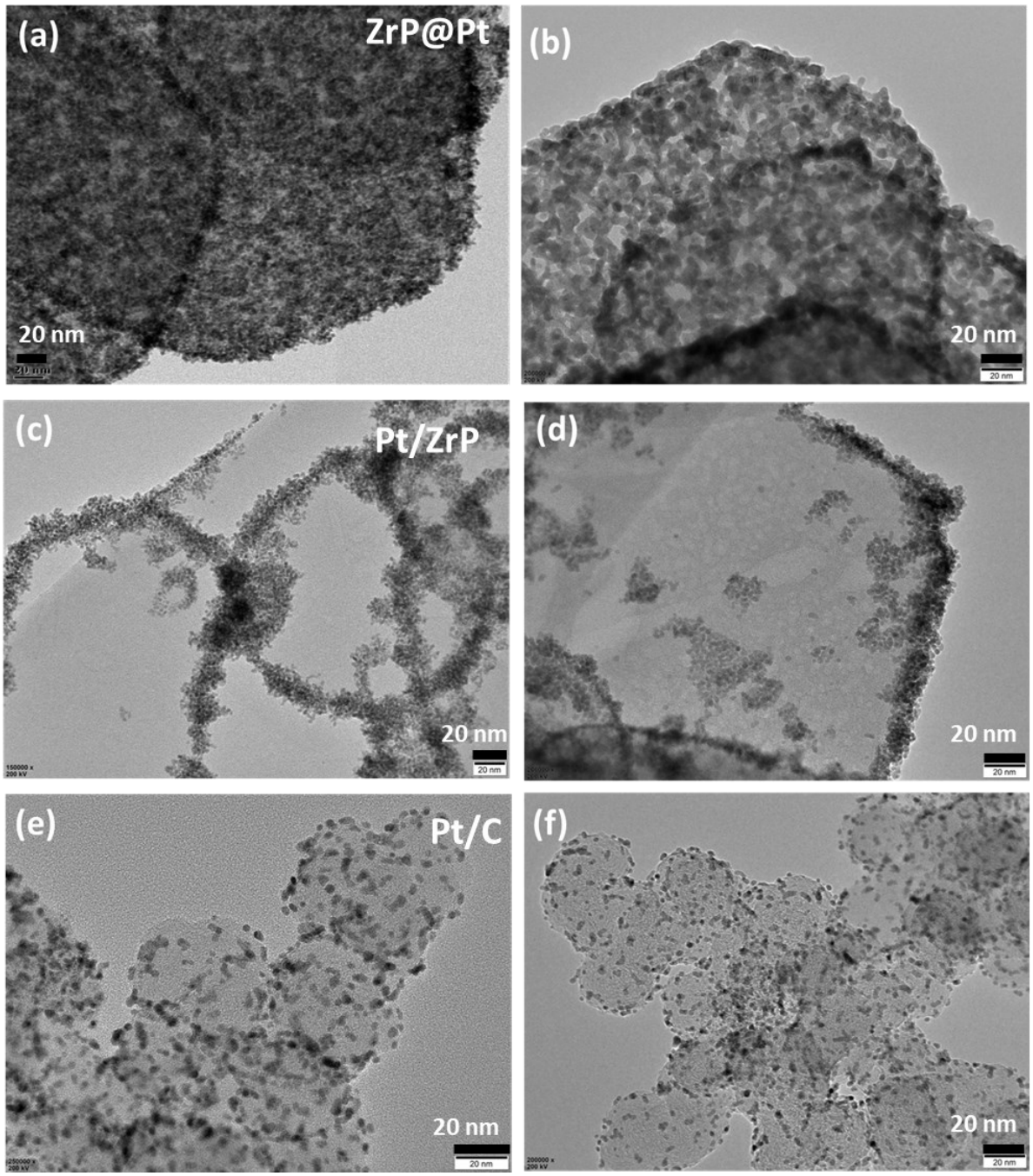

Figure S11. The TEM images of ZrP@Pt, Pt/ZrP, and Pt/C before (a, c, e) and after (b, d, f) ten days of aging at a pH 5.

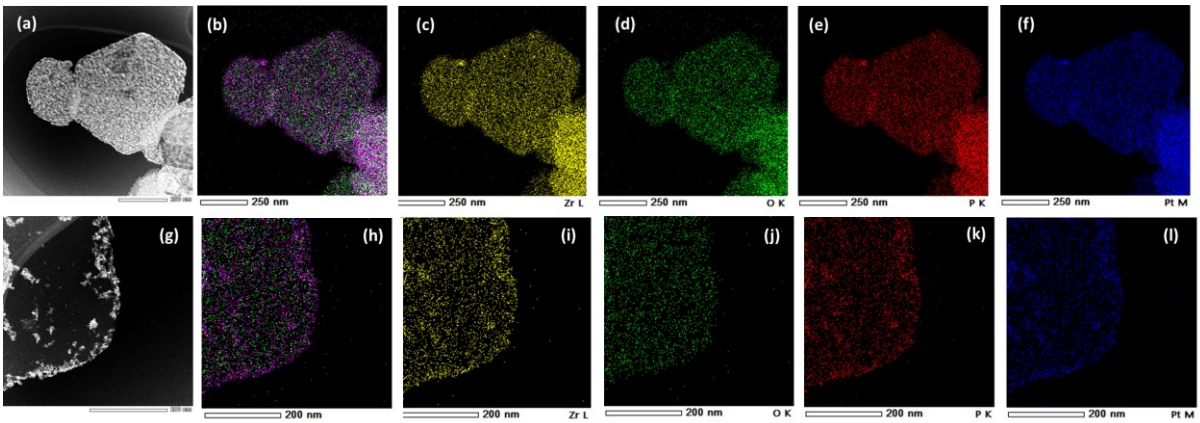

Figure S12. The HAADF-STEM and EDS mapping of Pt/ZrP (a-f) and ZrP@Pt (g-l).